

Earth and Space Science



RESEARCH ARTICLE

10.1029/2023EA002987

Key Points:

- A Geant4-based model has been developed to simulate radiation belt energetic particle precipitation (EPP)
- Mono-energy and mono-pitch angle beams are simulated to be combined using inversion methods to represent EPP quantities of interest
- Model results and inversion methods are validated using remote and in-situ measurements that compare favorably to modeled observations

Correspondence to:

G. D. Berland, grant.berland@colorado.edu

Citation:

Berland, G. D., Marshall, R. A., Capannolo, L., McCarthy, M. P., & Zheng, L. (2023). Kinetic modeling of radiation belt electrons with Geant4 to study energetic particle precipitation in Earth's atmosphere. *Earth and Space Science*, 10, e2023EA002987. https://doi. org/10.1029/2023EA002987

Received 17 APR 2023 Accepted 7 OCT 2023

Author Contributions:

Conceptualization: G. D. Berland, R. A. Marshall, M. P. McCarthy Data curation: G. D. Berland, L. Capannolo, M. P. McCarthy Formal analysis: G. D. Berland, L. Capannolo, M. P. McCarthy Funding acquisition: R. A. Marshall Investigation: G. D. Berland Methodology: G. D. Berland, R. A. Marshall, M. P. McCarthy, L. Zheng Project Administration: R. A. Marshall Resources: G. D. Berland, L. Capannolo Software: G. D. Berland Supervision: R. A. Marshall Validation: G. D. Berland, M. P. Visualization: G. D. Berland

© 2023 The Authors. Earth and Space Science published by Wiley Periodicals LLC on behalf of American Geophysical Union.

This is an open access article under the terms of the Creative Commons Attribution License, which permits use, distribution and reproduction in any medium, provided the original work is properly cited.

Kinetic Modeling of Radiation Belt Electrons With Geant4 to Study Energetic Particle Precipitation in Earth's Atmosphere

G. D. Berland¹, R. A. Marshall¹, L. Capannolo², M. P. McCarthy³, and L. Zheng³

¹Aerospace Engineering Sciences, University of Colorado Boulder, Boulder, CO, USA, ²Center for Space Physics, Boston University, Boston, MA, USA, ³Earth & Space Sciences, University of Washington, Seattle, WA, USA

Abstract We present a new model designed to simulate the process of energetic particle precipitation, a vital coupling mechanism from Earth's magnetosphere to its atmosphere. The atmospheric response, namely excess ionization in the upper and middle atmosphere, together with bremsstrahlung X-ray production, is calculated with kinetic particle simulations using the Geant4 Monte Carlo framework. Mono-energy and mono-pitch angle electron beams are simulated and combined using a Green's function approach to represent realistic electron spectra and pitch angle distributions. Results from this model include more accurate ionization profiles than previous analytical models, deeper photon penetration into the atmosphere than previous Monte Carlo model predictions, and predictions of backscatter fractions of loss cone electrons up to 40%. The model results are verified by comparison with previous precipitation modeling results, and validated using balloon X-ray measurements from the Balloon Array for RBSP Relativistic Electron Losses mission and backscattered electron energy and pitch angle measurements from the Electron Loss and Fields Investigation with a Spatio-Temporal Ambiguity-Resolving CubeSat mission. The model results and solution techniques are developed into a Python package for public use.

Plain Language Summary The upper atmosphere and near-Earth space interact with each other through the transport of charged particle (e.g., electrons) from space into the atmosphere in a process called energetic particle precipitation. This process disturbs the atmosphere and causes X-rays to be generated, among other direct and indirect effects to the atmosphere, including ozone destruction. This work describes a physics-based model that simulates this process across realistic input values for energy and electron velocity direction. Results of this work include an estimate of the number of excess ion-electron pairs generated in the atmosphere from precipitation, how many electrons are lost to the atmosphere versus those that rebound and return to space, and the energy and amount of X-rays generated by precipitation. The model outputs are checked using balloon-based measurements of X-rays in the middle atmosphere and by a low Earth orbiting satellite that spins to measure electrons heading toward and away from Earth.

1. Introduction

Energetic particle precipitation (EPP) is a coupling mechanism between Earth's magnetosphere and atmosphere wherein charged particles are lost from the magnetosphere and are subsequently deposited into the atmosphere. At Earth, this process for energetic electrons is sourced by the outer radiation belt which is composed of high intensities of energetic and relativistic electrons and is located approximately three–seven Earth radii from the Earth's surface at the equator (Akasofu & Chapman, 1961; Shprits et al., 2008). Within the radiation belts, plasma waves generate these relativistic populations by accelerating electrons from low energies (eV–keV) to relativistic and ultra-relativistic energies (100s keV–MeV electron kinetic energies) (Chen et al., 2007; Horne et al., 2005; Millan & Baker, 2012).

Plasma waves can also alter an electron's momentum direction relative to the magnetic field line (i.e., pitch angle) to be redirected into the "loss cone," which is the region of electron phase space that allows electrons to reach altitudes lower than 100 km. At these altitudes the electrons can interact with the neutral molecules in Earth's atmosphere and thus these electrons can be lost from the radiation belt population (Lyons et al., 1972; Sergeev et al., 1983; Summers & Thorne, 2003). Electrons spanning 10 s keV–MeV kinetic energies precipitate from the radiation belts due to magnetospheric plasma waves from a variety of natural and anthropogenic sources, including solar activity which drives geomagnetic storms and wave activity, atmospheric lightning, and Earth-based radio transmitters (Horne & Thorne, 2003; Horne et al., 2003; Lam et al., 2010).

BERLAND ET AL. 1 of 25

Writing – original draft: G. D. Berland Writing – review & editing: G. D. Berland, R. A. Marshall, L. Capannolo, M. P. McCarthy Electrons within the loss cone lose energy by scattering with neutral particles in the atmosphere, and when charged particles can no longer leave Earth's atmosphere the electron is considered lost or precipitated to the atmosphere. An additional consequence of this process is bremsstrahlung X-ray production, which occurs when a high energy electron scatters through the Coulomb field of an atomic nucleus and results in a fraction of the electron's kinetic energy being converted into an energetic photon (Bunkin & Fedorov, 1966; Koch & Motz, 1959). These photons are typically in the X-ray to gamma- ray energies (10 s keV–GeV) and can be used as a remote sensing proxy measurement for EPP (Imhof et al., 1974, 1985).

The model used in this work is built from the Geant4 (GEometry ANd Tracking) framework, a validated radiation and particle transport code originally developed at CERN (Agostinelli et al., 2003; Allison et al., 2006), in addition to an atmospheric and a magnetic field model. Initial conditions are chosen that cover a realistic range of energies and pitch angles, and the model then propagates and tracks the 3D trajectory and energy of a large number of electrons and generated photons as they interact with atmospheric neutral particles using the Monte Carlo method. The results from this model are used to compute derived products, such as atmospheric ionization rates, that are vital to atmospheric modeling (Funke et al., 2016; Mironova et al., 2015; Sinnhuber et al., 2012). Model results are verified by comparison with previous models, and validated with spacecraft and balloon data in case studies.

Further, this work expands on and updates previous models that perform similar calculations with improved cross section implementations, and includes photon and secondary ionization peaks. Finally, a Python software package is described that allows user access to these model outputs, as well as a multitude of the analysis and inversion techniques described in Sections 5 and 6.

2. Background

The radiation belt driving mechanisms of EPP, namely wave-particle interactions, occur in the entire magnetized region around Earth on short time scales, which makes it difficult to provide comprehensive measurements of waves and particles to constrain when and where EPP is occurring (R. Anderson et al., 1982; LaBelle & Treumann, 1988; Ni et al., 2016). In addition to the high spatial and temporal coverage that is needed to characterize EPP, high energy and angular resolution measurements are also required to determine the effects of plasma wave drivers on precipitating electron spectra and pitch angle distributions (Frank & Ackerson, 1971). For these reasons, EPP is difficult to observe directly and as a consequence, the drivers of EPP in the radiation belts and the relative importance of EPP in the atmosphere are known only indirectly.

One of the primary drivers of EPP are wave-particle interactions from plasma waves in Earth's magnetosphere, which include electromagnetic ion cyclotron (EMIC), whistler-mode chorus, hiss, lightning-generated whistlers, and other very-low frequency waves from Earth-based transmitters (Asikainen & Ruopsa, 2016; Glauert et al., 2014; Inan et al., 1988; McPherron, 1979; Pytte et al., 1976; Rodger et al., 2007). Some of these wave modes are generated by geomagnetic storm activity and space weather events, which lead to anisotropies in the energetic plasma, and are ultimately driven by solar activity (Baker et al., 2018; Engebretson et al., 2008; Schwenn, 2006). In general, electrons at 100s keV kinetic energies are typically resonant with whistler mode chorus waves, and at MeV energies with EMIC waves, two types of plasma waves that are detected in the inner magnetosphere and have been shown to be drivers of EPP (Horne & Thorne, 2003; Horne et al., 2003; Lam et al., 2010).

Once electrons have entered the atmosphere, EPP has important effects on the upper and middle atmosphere. The primary mode of energy loss of high energy electrons is through collisional interactions, or the "friction force" the atmosphere imparts on charged particles (e.g., Dwyer, 2004). Radiative collisions, such as the ones that generate X-ray photons, become relevant at electron kinetic energies of 100 s of keV, but do not greatly affect the overall stopping power. Through scattering interactions between free electrons and neutral atmospheric particles, the neutrals can become ionized: impact ionization is among these scattering processes that yields excess electron-ion pairs generated from neutral species, enhancing the ionospheric electron and ion densities (Kim et al., 1997). The bulk effect is that EPP alters the chemistry balance, leading to excess NO_x and HO_x production, the former of which goes on to be transported to lower altitudes near the poles where it catalytically destroys ozone (M. Andersson et al., 2014; Codrescu et al., 1997; Mironova et al., 2015; Seppälä et al., 2007; Sinnhuber et al., 2012; Thorne, 1980). Additionally, excess ionization alters the conductivity of the ionosphere and further alters the geomagnetic current systems that couple the atmosphere and magnetosphere (Khazanov et al., 2018; Ridley et al., 2004).

BERLAND ET AL. 2 of 25

In atmospheric models, EPP is typically addressed via parameterized inputs in order to save on computation speed in exchange for event specificity. Typical quantities that are used to characterize precipitation are some measure of flux (e.g., number flux, energy flux) and energy spectrum, or parameter(s) that describe the spectrum, such as a folding energy for an exponential distribution. The early work of R. G. Roble and Ridley (1987) used an analytical approach using the electron stopping power formulation to characterize auroral precipitation inputs for the thermospheric general circulation model, while the work of Berger and Seltzer (1972) and Berger et al. (1974) used Monte Carlo methods to study bremsstrahlung photon penetration into the atmosphere. Frahm et al. (1997) calculates atmospheric ionization rates by including electrons and secondary photons using a Boltzmann transport equation multi-stream model, based off the model of Lorence and Morel (1992). The improved analytical model of Fang et al. (2008, 2010) was created for convenient use in "high top" whole atmosphere models such as WACCM-X that extend to the mesosphere and above (Liu et al., 2018). This analytical model forward-models mono-energy beams with isotropic pitch angle distributions that an end user can combine to represent an arbitrary continuous and smooth spectrum. Finally, the work of Xu et al. (2020) uses a full Monte Carlo model with forward-modeled mono-energy and mono-pitch angle electron beams that more realistically represents high energy processes, but does not include bremsstrahlung transport to lower altitudes. Bremsstrahlung transport is shown for three energies in Xu et al. (2021): the last two of these previous works are directly compared to this work in Section 6. Other models exist that use similar Monte Carlo techniques for different purposes, such as the auroral model of Solomon (2001).

Radar remote sensing of excess ionization in the ionospheric D- and E- regions is difficult due to high atmospheric neutral density driving fast recombination, which causes ionization enhancements to dissipate quickly. Atmospheric effects can be measured as a proxy to precipitation inputs, but the complicated chemistry and transport dynamics makes the inversion to precipitation characteristics difficult and uncertain (Marshall & Cully, 2020). On the other hand, direct in situ measurements of charged particles from spacecraft have difficulty obtaining the spatial and temporal coverage due to the aforementioned large spatial scales of EPP and the nature of low-Earth orbits. Additionally, charged particle instruments are often angular resolution-limited and are therefore unable to resolve the loss cone at various points in the orbit, which is necessary to provide a global image of precipitation (Blum & Breneman, 2020; Capannolo et al., 2021).

In order to obtain global measurements of EPP, remote measurements of X- and gamma- ray photons can instead be used to infer EPP over larger spatial scales. Bremsstrahlung photon energy and emission direction is strongly dependent on the precipitating electron energy, such that statistical relationships can be formed between the X-ray and electron spectra. A component of this work is to prepare for future hard X-ray observation missions of Earth to quantify the extent of radiation belt EPP, such as the upcoming Atmospheric Effects of Precipitation through Energetic X-rays CubeSat mission (Marshall et al., 2020). A variety of information can be garnered on EPP from inverting X-ray spectral measurements of Earth from low Earth orbit or from balloon measurements, where a review of the former, X-ray observations from space, is included in Berland et al. (2023) for Earth and Bhardwaj et al. (2007) for other planets.

Open questions of magnetosphere-atmosphere coupling primarily relate to the wave particle interaction driving mechanism of EPP: how does EPP vary seasonally, temporally, and with magnetospheric conditions; and what are the spatial scales over which this process occurs? The answers to these questions will help constrain the total energy budget of the radiation belts and atmosphere, and lend a deeper understanding of the dynamic interactions between Earth's magnetosphere and atmosphere. For a review of EPP open questions, see Marshall et al. (2020).

3. Model Description

This work aims to explore an input space composed of electron pitch angle and energy distribution through various radiation belt magnetic latitudes using the EPP model described in this section. The range of magnetic latitudes describe the atmospheric profiles and magnetic dip angle, both of which change the linear distance that an electron will travel through a given atmospheric density, effectively increasing the integrated column density that an electron will traverse. In order to explore these continuous input spaces, the approach of Fang et al. (2010) and Xu et al. (2020) is taken by simulating a finite number of mono-energy and mono-pitch angle electrons beams through a reference atmosphere at one magnetic dip angle. In order to convert model results to a different atmospheric profile, a rescaling method similar to Xu et al. (2020) is described and implemented in Section 4.

BERLAND ET AL. 3 of 25

The mono-energy, mono-pitch angle beams can be weighted and linearly combined using a Green's function approach. Green's functions are maps from Dirac delta function in an input space to the subsequent impulse response in an output space that can be used to solve boundary value problems in a variety of fields (Melnikov, 1977; Stakgold & Holst, 2011). In this work, we use the Monte Carlo forward method to approximate the Green's functions instead of finding an analytical form, which is difficult due to the rarefied and stochastic interactions that occur between high energy electrons and neutral particles. This method is discussed and formalized in Section 5.

The geometry of the model is a 500 km tall $\times 1,000 \text{ km}$ diameter 3D column that is filled with the MSIS2.0 (Mass Spectrometer Incoherent Scatter Radar-Empirical) model atmosphere, which includes the atmospheric state (temperature, pressure, density) and constituent number densities, taken at 1 km intervals (Picone et al., 2002). MSIS2.0 takes as inputs the F10.7 and A_n indices, which are solar and geomagnetic indices, respectively. F10.7 is a measurement of solar radio flux at the 10.7 cm wavelength, which has historically been used as a proxy measurement for solar extreme ultraviolet flux, which largely affects the scale height in the diffusive region of Earth's atmosphere above 100 km altitude (e.g., Tapping, 2013). The A_n index is derived from a measurement of the planetary K-index, which estimates solar particle flux through its magnetic effects on the inner magnetosphere (e.g., Fraser-Smith, 1972). The influence of these parameters on the atmospheric profile generated are in the atmospheric species scale heights: the scale heights affect the altitude distribution of constituents and the altitude of constant pressure surfaces in the atmosphere primarily above 100 km altitude, but since only a small fraction of relativistic electron energy is lost above 100 km, these two parameters do not have a strong influence on the results of this work. The geomagnetic parameters are selected for the corresponding date-time chosen for this atmospheric profile, during a geomagnetic "quiet time" with $A_n = 22$ (corresponding to a $K_n = 4$) and F10.7 = 66.8 sfu (solar flux units). The location for the reference atmosphere profile selected is over the Poker Flat Incoherent Scatter Radar (PFISR) station located in Alaska at 65° North latitude 147° West longitude, at midnight local time.

A tilted dipole magnetic field is used to model the near-Earth magnetic field vector since the field only varies on the order of 2% at 500 km from a higher fidelity magnetic model such as the International Geomagnetic Reference Field (Alken et al., 2021). An important aspect of the geometry of EPP is the additional path length an electron must travel due to the local magnetic inclination at a given latitude. The magnetic inclination θ_i , defined as $\tan(\theta_i) = B_i/B_\theta$, at PFISR is approximately 78°, or 12° away from the vertical. Until the electron's motion is dominated by collisions, the guiding center of the cyclotron motion will follow the magnetic field line, adding an additional factor of $\sec(\pi/2 - \theta_i)$ to the path length the electron travels through the atmosphere. The magnetic latitudes of 45° (L = 2) and 90° ($B_\theta = 0$) where the inclinations are 64° and 90°, respectively, are also simulated to analyze the effects of varying magnetic dip angle through all magnetic latitudes where precipitation most often occurs.

In the simulation electrons are injected equidistant from the walls of the simulation volume at 300 km altitude, where the loss cone edge is approximately 73° and with electron pitch angles defined relative to the inclined magnetic field. The simulation volume is sufficiently large enough that very few particles (<0.1%) leave the simulation volume, and those electrons or photons that do leave have their remaining energy deposited at their last altitude step in order to conserve the total energy input into the simulation volume. The resulting electron and photon backscatter are tracked until 500 km altitude, where they are sufficiently above the neutral atmosphere to be considered escaped from the atmosphere. An example of the general pitch angle and energy dynamics of a single particle with various initial conditions is shown using analytical approximations in Figure 1. In this figure, the electrons are started at a higher altitude of 500 km where the loss cone edge is at 66°, and the progression to lower pitch angles shows that- if not for the effects of atmospheric backscatter- electrons more than a few degrees away from the edge of the loss cone must surely precipitate. The assumption that the entire population of the loss cone precipitates is challenged by simulation results in Section 4 and by in situ electron data in Section 6.3.

The forward model selected for this work is built from Geant4, a radiation and charged particle transport code originally developed at CERN for high energy physics (Agostinelli et al., 2003; Allison et al., 2006). Geant4 is a collection of C++ classes and implementations that allow for modular creation of physics simulations with arbitrary geometries and materials, types of charged particles and photons, and a list of physical processes and cross sections to simulate. A variety of cross section implementations and scattering models, called physics lists, have been developed for a variety of applications including the space radiation environment (Ersmark et al., 2007; Truscott et al., 2000). For this simulation work, we choose the validated QBBC physics list, which itself is a collection of previous validated scattering cross sections and model implementations (Ivanchenko et al., 2010).

BERLAND ET AL. 4 of 25

23335084, 2023, 11, Downloaded from https://agupubs.onlinelibrary.wiley.com/doi/10.1029/2023EA002987, Wiley Online Library on [20/08/2024]. See the Terms and Condition of the C

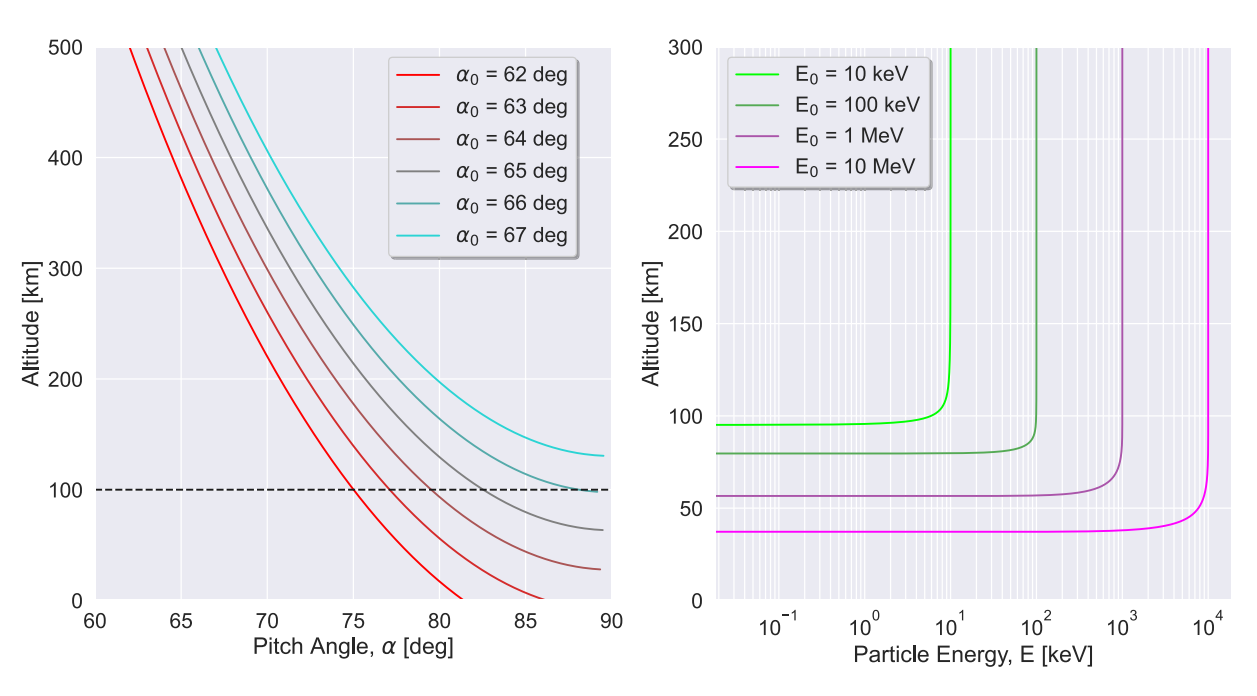


Figure 1. (Left) Single particle pitch angle evolution with altitude, where α_0 is the pitch angle at 500 km altitude. The black dashed line marks 100 km, which is the altitude used to define the edge of the loss cone. (Right) Energy evolution with altitude from electrons injected at field-aligned pitch angles using continuous slowing down approximation stopping power. Highlighted here is the relative depth of penetration into the atmosphere with initial particle energy.

Included in this simulation are the effects of impact ionization including single, double, K-shell ionization, etc. that are ultimately determined via the Møller electron-electron scattering cross sections (Mark, 1982). For the electron energies considered by this work, Geant4 implements the Livermore low-energy electromagnetic model, which includes validated cross sections and implementations for electron ionization and bremsstrahlung, the photoelectric effect, and Compton scattering from 250 eV–100 GeV, and pair production from 1,022 keV ($2 \times$ electron rest energy)–100 GeV (Ivanchenko et al., 2011). For electron multiple scattering effects through matter the Urban, Wentzel VI, and Coloumb scattering models are implemented which include angular diffusion (Ivanchenko et al., 2010; Urban, 2002).

For electron angular diffusion, Geant4 implements the Goudsmit-Saunderson model, which parameterizes the multiple Coulomb scattering physics that primarily affect precipitating electrons below 100 km altitude (Ivanchenko et al., 2010). For thin-target bremsstrahlung photon production, the Seltzer-Berger model is implemented (Berger & Seltzer, 1972; Seltzer & Berger, 1986). A comparison between bremsstrahlung cross section implementations, including the cross section model used in Xu et al. (2020), is presented in Köhn and Ebert (2014). The bremsstrahlung cross section becomes more dominant at higher energies (MeV electron kinetic energies), so it is a rare process at lower energies. For this reason, a statistical biasing method is implemented to better inspect photon production via the bremsstrahlung interaction for simulation energies below 500 keV. This method samples the bremsstrahlung cross section N_{brems} times for every time a photon would be generated and assigns a weight of $1/N_{brems}$ to every subsequent photon and secondary particle scoring quantity, such as energy deposition (e.g., Ivanchenko et al., 2014; Tinslay et al., 2007). In this study an N_{brems} value of 100 is used to smooth the X-ray spectral distributions. Figure 2 shows the influence of this method on the quality of the results, with particular benefit for X-ray propagation at lower altitudes.

The energy range selected corresponds to realistic energies characteristic of the outer radiation belt (Li & Temerin, 2001; Whittaker et al., 2013). The simulations implement energy via a monoenergetic beam, with energies spaced approximately logarithmically from 10 keV to 10 MeV. A variety of energy distributions can be evaluated using these beam energies as control points and using the corresponding normalized function value as a weight to apply to a linear summation. This same method can be performed with mono-pitch angle beams to reproduce arbitrary pitch angle distributions. This method is formalized via Green's function analysis in Section 5 for various quantities of interest, including atmospheric ionization rate. Additionally, in order to obtain various quantities of interest from this model, a series of conversion factors is needed to relate the model outputs to

BERLAND ET AL. 5 of 25

23335084, 2023, 11, Downloaded from https://agupubs.onlinelibrary.wiley.com/doi/10.1029/2023EA002987, Wiley Online Library on [20/08/2024]. See the Terms and Conditions (https://onlinelibrary.wiley.com/terms-and-conditions) on Wiley Online Library for rules of use; OA articles

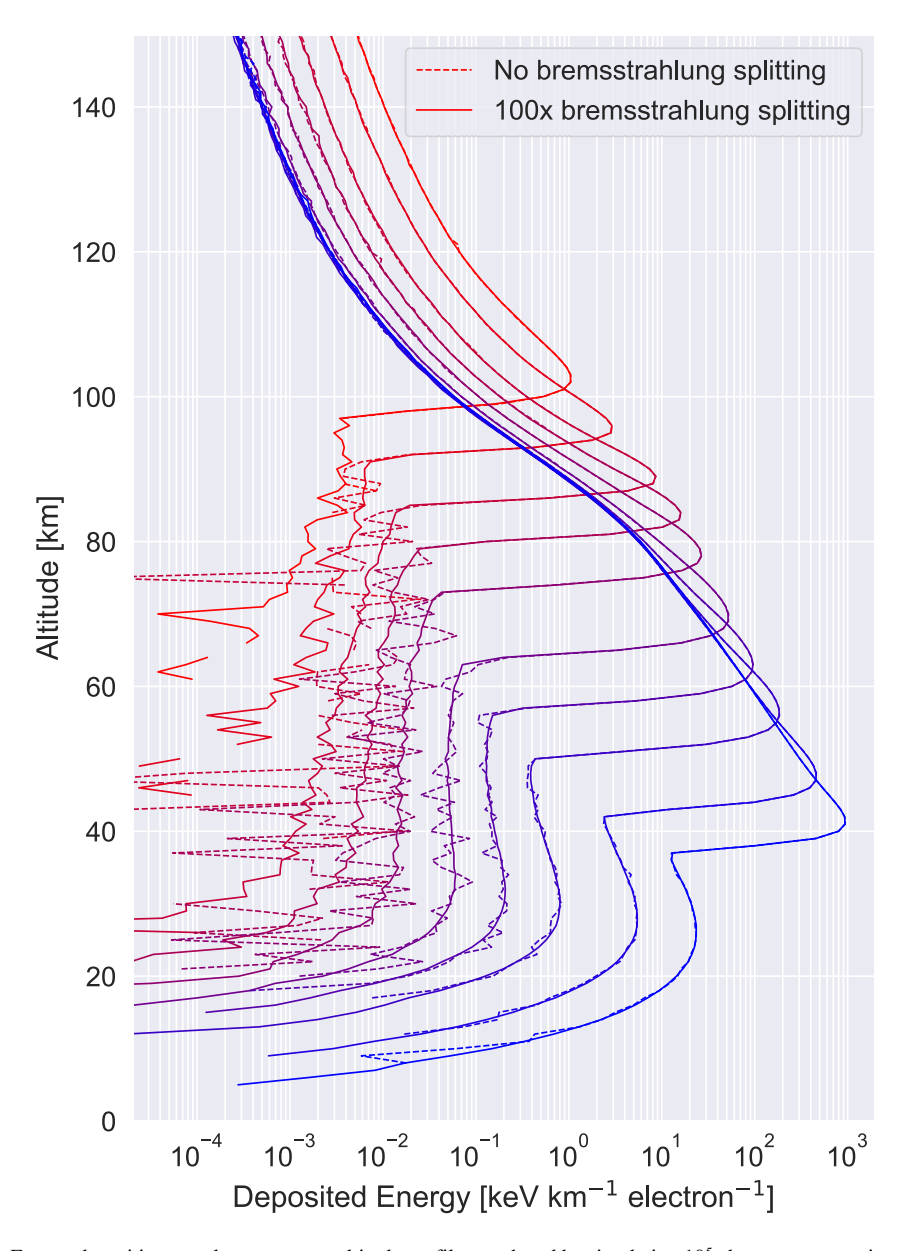


Figure 2. Energy deposition per electron versus altitude profiles produced by simulating 10^5 electrons at energies of 10, 20, 50, 100, 200, 500, 1,000, 2,000, 5,000, 10,000 keV (red to blue). Each profile is run with a $100 \times$ numerical bias toward bremsstrahlung enabled. A comparison with and without the biasing method is shown here using an isotropic pitch angle distribution.

physical quantities. These conversion factors relate energy deposition to ionization and number of particles run in the simulation to flux units, and are described below.

A conversion factor is needed to relate energy deposition rate in the atmosphere to atmospheric neutral ionization rate. In the work of Fang et al. (2008) and Xu et al. (2020) an average first ionization energy of air, denoted in this work by η , from electrons transiting a unit distance is assumed to be a constant 35 eV cm pair⁻¹, however the average first ionization potential of a mixed gas is a function of gas mixing ratios and therefore of altitude in the atmosphere. An alternative to the constant ionization potential assumption are the simulation results of Krause (1998) where a relativistic electron beam is simulated through the atmosphere. It's found that an affine function of the following form provides a better estimate for ionization in the atmosphere:

$$\eta(h) = \eta_0 + \frac{\partial \eta}{\partial h} \cdot h \tag{1}$$

BERLAND ET AL. 6 of 25

valid for altitudes h between 45 and 240 km, with $\eta_0 = 39.78$ eV cm pair⁻¹ and a slope parameter of $\partial \eta/\partial h = -0.03$ eV cm pair⁻¹ km⁻¹. This formulation yields ionization energies that vary up to 10% from the constant 35 eV cm pair⁻¹ assumption, but more importantly the ionization rate conversion is now a function of altitude, so the shape of the altitudinal ionization profile is affected. For simplicity, the results shown herein use the constant 35 eV cm pair⁻¹ conversion and the software package described in Section 7 enables the conversion factor described by Equation 1 for higher accuracy.

In order to translate the number of particles run N_p in the simulation to a differential flux unit, a conversion factor is needed. If we simply want total flux, that is, cm⁻² s⁻¹, we can choose an effective detection area ΔA_d and time interval Δt to be unity, that is to say 1 cm² and 1 s, respectively, such that the number of particles run in the simulation can be related to the number flux of electrons. However if we want to express our flux differentially in angle space, an additional conversion factor is needed given the initial input pitch angle. In this work, we take the equation

$$N_p = -dt \ d\Omega_d \ \left(f(\hat{k}_s) \ \hat{k}_s \right) \cdot \left(dA_d \ \hat{k}_d \ \right) \left[\hat{k}_s \cdot \hat{k}_d < 0 \right] \tag{2}$$

where $d\Omega_d$ is the differential solid angle that couples the simulation geometry and distribution momentum direction, $f(\hat{k}_s)$ \hat{k}_s is the electron distribution in phase space, with momentum space vector \hat{k}_s , dA_d describes the differential geometry of the simulation surface with outwards surface normal \hat{k}_d , dt is the time in which electrons pass through the surface dA_d , and the bracketed term is the indicator function. The negative sign and indicator function term enforce inwards directionality to particles on the surface of the simulation. We can express the dot product between the momentum direction of the beam and surface normal as a function of mono pitch angle α_0 : \hat{k}_s $\hat{k}_d = \cos(\alpha_0)$ in order to obtain the relationship between number of particles simulated and differential flux in terms of integral flux f_0 . Finally, the indicator function restricts the limits of integration to $\pi/2$ to remove the effect of anti-Earthward directed electrons:

$$\frac{N_p}{dt \ dA_d} = f_0 \int_0^{2\pi} \int_0^{\pi/2} \cos(\alpha_0) \sin(\alpha) \ d\alpha \ d\theta \tag{3}$$

The conversion factor from integrating over the hemisphere is then purely a function of the angle at which the beam is directed through the simulation surface normal:

$$f_0 = \frac{1}{2\pi \cos(\alpha_0)} \frac{N_p}{dt \ dA_d} \tag{4}$$

which represents the relationship between a desired differential flux in units of cm⁻² s⁻¹ sr⁻¹ from N_p particles run in a simulation at mono-pitch angle α_0 . When the beam is field-aligned, the normalization factor is 2π and the conversion factor is also well behaved at $\alpha_0 = 90^\circ$ since the number of particles passing through the simulation surface N_p vanishes at that angle. Once properly normalized, the flux can be scaled multiplicatively since we assume EPP is a linear process, that is, electrons do not sufficiently interact with each other. Further, this flux can be made differential in energy by multiplying with an energy distribution function in units of keV⁻¹ that integrates to unity.

The Geant4 model is run on a supercomputer across five nodes using 40 cores per node, parallelized across one thread per core. In order to evaluate variation information for a given simulation, 10^5 particles are split evenly between 40 simulation threads in order to produce histograms from 2,500 electrons/thread. The sample standard deviation is calculated across the 40 output histograms and we conclude a sufficient number of particles have been simulated since the standard deviation varies less than 0.01% from the mean. The 40 histograms are then summed and divided by the number of particles run, in addition to the conversion factor described in the previous section, to convert to differential flux units. The runtime for the full simulations are on the order of 3–4 days for a run with 19 energies \times 15 pitch angles, with the higher pitch angle simulations taking significant more time than lower pitch angles due to the longer path length traversed by those electrons.

The methods described in this section are a description of the treatments applied to the raw data output by the model, which include histograms of: (a) weighted energy deposition per altitude bin, (b) a particle's weighted energy passing through a 2D energy-altitude bin, and (c) pitch angle and energy recorded at 500 km. These outputs and their physical meanings are discussed in the next section.

BERLAND ET AL. 7 of 25

2335084, 2023, 11, Downloaded from https://agupubs.onlinelibrary.wiley.com/doi/10.1029/2023EA002987, Wiley Online Library on [20/08/2024]. See the Terms and Conditions (https://onlinelibrary.wiley.com/terms-and-

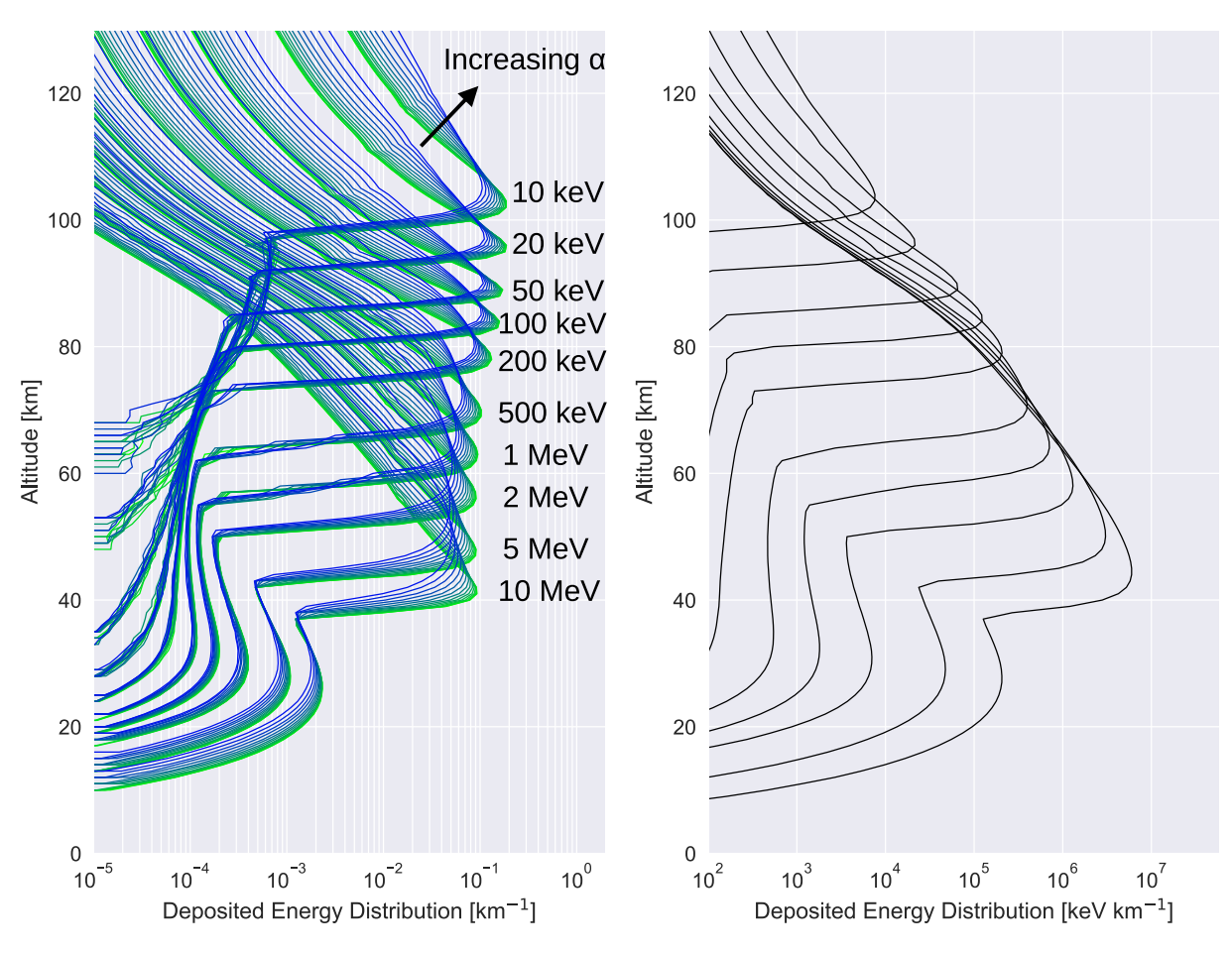


Figure 3. (Left) Green's function energy deposition (proportional to ionization rate) response to mono-energy mono-pitch angle inputs, normalized to integrate to unity. Variation in pitch angle from field-aligned (0°, green) to near the edge of the loss cone (70°, blue) is shown, at pitch angle spacing $\Delta \alpha = 5^{\circ}$ and variation in pseudo-log-spaced energies denoted on the plot, with peaks descending in altitude. (Right) Mono-energy, sine pitch angle distribution inputs, energy deposition profiles showing the relative energy deposited per input beam. These profiles are normalized to 10^4 precipitating particles at each energy.

4. Model Results

The first primary outputs from the simulation are altitude distributions of energy deposition into the atmosphere, shown in the left plot of Figure 3. The right plot of this figure shows the results of a single energy E_0 and pitch angle α_0 profile normalized by the input energy flux so that they integrate to unity. The right plot of Figure 3 shows the same profiles but weighted by a sine function in pitch angle in order to show the relative amount of energy deposited per mono-energy beam. These profiles can be directly converted into ionization rate using either a constant 35 eV cm/pair assumption or, for higher accuracy, the conversion factor described by Equation 1. The input energy is varied from 10 keV to 10 MeV using 19 pseudo-logarithmically spaced points and the input pitch angle at 300 km is varied from 0° to 70° with $\Delta\alpha = 5^{\circ}$ resolution, which extends near the edge of the loss cone at 300 km of 73° . These profiles are the basis functions $G(E, E_i, \alpha, \alpha_j)$ of the Green's functions method and can be combined to estimate ionization from an arbitrary input electron spectrum and pitch angle distribution.

Two main features stand out in Figure 3. First, a small variation in peak ionization altitude $h(I_{\rm max})$ with pitch angle is evident, with more field-aligned pitch angles depositing slightly lower in the atmosphere and with a sharper ionization peak. Secondly, the main source of variation is with beam energy, where the altitude of peak ionization descends about 20 km per decade of beam energy increase, with a slight pitch angle dependence: this variation in altitude of maximum ionization is shown in Figure 4.

The second set of primary outputs from the simulation is composed of altitude-energy histograms that are processed using the conversion factor in Equation 4 to produce number flux of electron and photon species at 1 km steps from 10^{0} – 10^{4} keV in 100 logarithmically spaced bins. Figure 5 shows beam energies of 500 keV and

BERLAND ET AL. 8 of 25

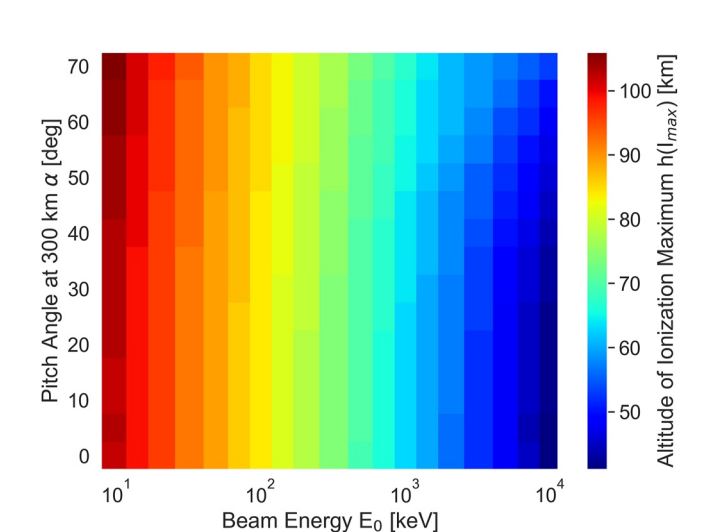


Figure 4. Altitudes of maximum ionization for mono-energy, mono-pitch angle electron beams versus the input beam energy and pitch angle. A strong dependence on input beam energy and a weaker dependence on input pitch angle is shown.

5 MeV, both of which are averaged with identical weights over pitch angle (i.e., an isotropic pitch angle distribution). The transition region where the majority of the main electron beam flux is converted into secondary electron and photon flux in a small altitude window is a function of beam energy and is at approximately 65 km for 500 keV and 45 km for 5 MeV in Figure 5, which is reflected in the energy deposition profiles as well. From that primary peak and below, the energy is transported Earthwards via electromagnetic shower, where a primary electron creates a bremsstrahlung photon which propagates and creates a free electron from Compton scattering, which itself can be of substantial energy to create another bremsstrahlung photon, until the energy from this cycle is absorbed into the atmosphere. At beam energies approximately greater than 200 keV this phenomenon tends to create a coherent secondary ionization peak at lower altitudes. The magnitude of the lower, secondary peak is proportional to the magnitude of the primary peak, as well as the initial beam energy. Additionally, due to the rapid evolution of the photoelectric cross section at low photon energies, a portion of the altitudinal photon spectrum is strongly attenuated at energies below ~30 keV, which presents as the "bite" taken out of the lower left corners of the photon spectra in Figure 5.

In addition to observing the precipitation process through altitude and energy, these histograms can be used to create secondary or derived simula-

tion outputs. The first derived output is electron and photon backscatter, which can be inferred from the results at the top of the model since 500 km is sufficiently above the neutral atmosphere for electrons to be considered reentering purely magnetized motion and ray-like propagation paths for photons. Figure 6 shows the backscatter efficiency in electron number flux, including the effects of secondary production (such that the percentage of backscattered particles can theoretically exceed 100%), over input beam energy and pitch angle. The second derived output is electron and X-ray spectra at any specified altitude, which can be obtained by averaging over a slice of the histogram in altitude. The minimum altitude resolution for any derived output is the 1 km bin size directly output by the simulation.

The energy and pitch angle of atmospherically backscattered electrons at 500 km altitude is recorded in order to evaluate the coupled energy-pitch angle distribution. This work supports the conclusions of the modeling performed in Marshall and Bortnik (2018) where a dependence on electron energy and pitch angle to precipitation likelihood is found. An interesting implication of Figure 7 is that a portion of the backscattered flux re-enters the trapped region and will not necessarily precipitate on subsequent bounces into the conjugate hemisphere. These particles backscattered into the trapped population above 100 km altitude such that they remain trapped unless acted upon by wave-particle interactions further out in the magnetosphere. The phenomenon of re-entry to the trapped population is more likely for electrons with high initial pitch angles.

By averaging a slice of the photon altitude-energy spectrum in altitude, such as the histograms in Figure 5, we can obtain X-ray spectra at various altitudes. Figure 8 shows the average X-ray spectrum over 25–35 km and over 250–300 km for a range of simulation energies. This derived product is especially useful since X-rays can be used as an observable for precipitation inversion problems, such as the case study in Section 6.2. The characteristically peaked shape of the bremsstrahlung X-ray distribution at 60 keV is a product of the composition of Earth's atmosphere and the electron-neutral bremsstrahlung cross section, and is therefore somewhat consistent across a wide range of energies and altitudes. The change in the slope of the high-energy tail of the photon distribution is indicative of the driving electron spectrum at all altitudes, in addition to the total number of photons produced since bremsstrahlung efficiency is energy-dependent. Above the atmosphere, the slope of both the high and low energy tails can be related to the driving electron spectrum.

Other notable features of Figure 8 include absorption of the lower energy portion (<20 keV) of the X-ray spectrum before that portion of the spectrum can propagate to altitudes lower than ~40 km, which is shown in Figure 5 and supported by the work of Frahm et al. (1997) as well as observations from Balloon Array for RBSP Relativistic Electron Losses (BARREL). This effect, in addition to instrument limitations, poses a difficulty to balloon missions aiming to measure the X-ray spectrum as the <20 keV portion of the spectrum includes important

BERLAND ET AL. 9 of 25

2335/084, 2023, 11, Downloaded from https://agupubs.onlinelibrary.wiley.com/doi/10.1029/2023EA002987, Wiley Online Library on [20/08/2024]. See the Terms and Conditions (https://onlinelibrary.wiley.com/terms-and-conditions) on Wiley Online Library for rules

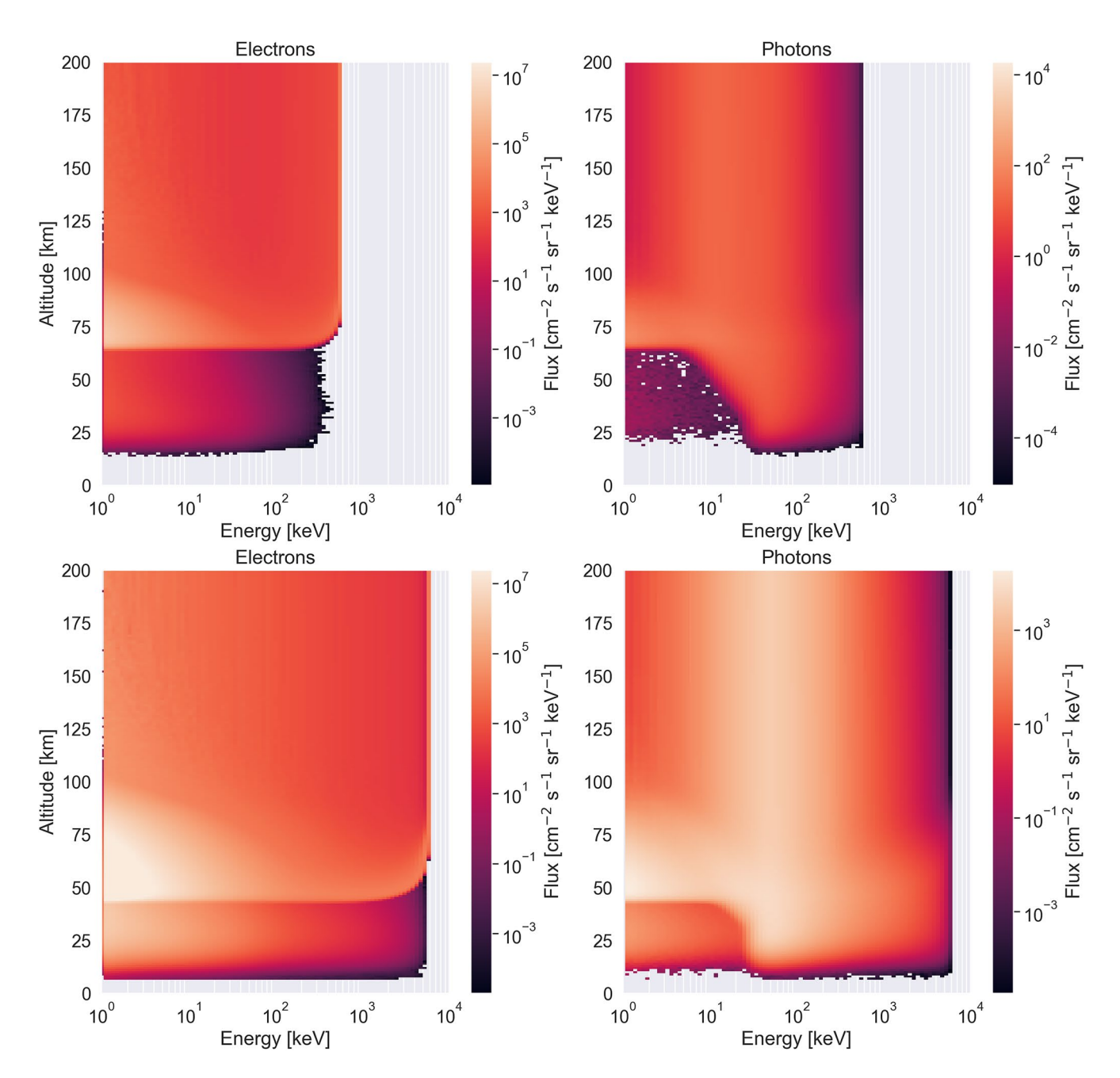


Figure 5. Altitude-energy histogram plots of number flux from (top row) a 500 keV and (bottom row) 5 MeV electron beam at an isotropic pitch angle distribution, showing (left column) electron flux and (right column) photon flux. The input flux for both energies is $10^4 \, \mathrm{cm}^{-2} \, \mathrm{s}^{-1} \, \mathrm{sr}^{-1} \, \mathrm{keV}^{-1}$.

information on the precipitating electrons. X-ray spectra and electron pitch angle are not clearly related; the major effect seen in the X-ray spectrum by varying pitch angle is in the number of electrons available to produce bremsstrahlung X-rays at a given altitude. Therefore, higher pitch angle electron inputs have higher backscatter rates and do not reach as low in altitude as low pitch angle inputs. This in turn reduces X-ray production and requires X-rays to transit a longer path length through the atmosphere to reach balloon altitudes, which can further attenuate the low energy portion of the X-ray spectra that reach these altitudes.

Finally, we investigate the effect of the inclination of the magnetic field on ionization profile. The extra distance traveled by an electron through the atmosphere can be found at a geomagnetic latitude λ with the expression for inclination θ_i in a dipole field

$$tan(\theta_i) = 2tan(\lambda) \tag{5}$$

BERLAND ET AL. 10 of 25

23335084, 2023, 11, Downloaded from https://agupu

.com/doi/10.1029/2023EA002987, Wiley Online Library on [20/08/2024]. See the Terms

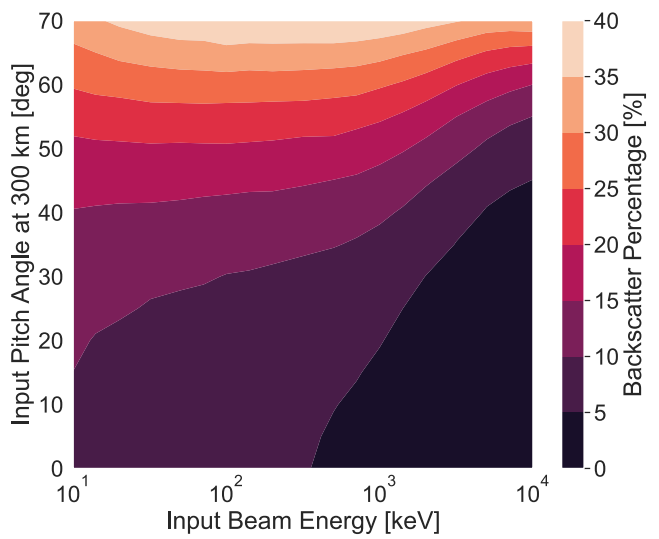


Figure 6. Total backscatter from with an input beam energy E_0 and pitch angle α_0 at injection altitude 300 km. At low energies and high pitch angles, only 2/3 of the loss cone population is precipitating in one bounce interaction with the atmosphere.

which can be used to calculate the excess distance traveled by an electron along a magnetic field line, relative to the vertical: $\sec(\pi/2 - \tan^{-1}(2\tan(\lambda)))$. At the lower limit of the latitude investigated at 45° the extra distance traveled relative to a purely vertical magnetic field is approximately 12%.

These effects are compared to the variation that occurs from atmospheric profile variation with latitude. An atmospheric rescaling method is used in this work which involves a remapping of the ionization profile according to the cumulative integral of the atmospheric density (Xu et al., 2020). It's found that the variation of the ionization profile due to magnetic inclination is small relative to the variation of the atmosphere with latitude, which has a more significant effect on the ionization profile.

5. Forward and Inverse Methods to Estimate Precipitation Characteristics

A key application for this model is in the generation of observable quantities for the largely unobservable geometry of EPP. Enhanced ionization rates (or indirect effects from these perturbations) and X-ray photons are two of the primary ways that EPP is measured indirectly. This section provides a framework to relate the results from this model to realistic electron energy and pitch angle distributions.

The simulation input space is a series of mono-energetic and mono-pitch angle beams $\delta(E-E_i,\alpha-\alpha_j)$ at electron beam energy E_i and input pitch angle at 300 km α_j , from which we can use a Green's function method to solve an inverse problem; that is to say, we want to estimate the initial condition at the top simulation boundary given observations (measured or simulated) from within the simulation volume. A similar approach is taken in Xu and Marshall (2019) and Patrick (2022). The formalism used here is similar to Omura et al. (2015): we take EPP to be a linear process, that is, there is no self-interaction within the electron beam and the neutral atmospheric state is not modified significantly with an impulse of precipitation. We then write the process of atmospheric response (e.g., X-ray production, ionization) as a linear differential operator \mathcal{L} that operates on a quantity of interest u(x, h) at altitude h in response to precipitation forcing spectrum $f(E, \alpha)$ that describes electron spectral and pitch angle distribution. For example, we can take the differential bremsstrahlung X-ray spectrum $u(E_\gamma)$ at a given altitude as our quantity of interest, where E_γ is the photon energy:

$$\mathcal{L}[u(E_{\gamma})] = f(E, \ \alpha) \tag{6}$$

which by ansatz we assume has an integrable Green's function $G(E_i, \alpha_j, E_\gamma)$ relating an impulse in the electron energy and pitch angle space to an output in X-ray spectral space, from which we can formulate an inversion problem to estimate f given u:

$$\mathcal{L} [G] = \delta \tag{7}$$

$$\mathcal{L}^{-1}[\delta(E - E_i, \alpha - \alpha_j)] = G(E_i, \alpha_j, E_\gamma)$$
(8)

Since we now have the Green's functions from the Geant4 simulation for a variety of input (E_i, α_j) , we can decompose our source spectrum $f(E, \alpha)$ as a summation of Dirac delta functions, each with differential intensity from the Green's function coefficient matrix S_{ij} :

$$f(E,\alpha) \approx \sum_{i=1}^{N} \sum_{j=1}^{M} S_{ij} \ \delta(E - E_i, \ \alpha - \alpha_j)$$
 (9)

where the two sides are equal in the limit of $N, M \to \infty$. In this case, N and M are the number of energy and pitch angle bins, respectively. We can form the beam intensities by evaluating a spectrum of interest, for example, an exponential energy distribution with folding energy E_0 and sine pitch angle distribution, $S_{ii} \propto \exp(E_i/E_0) \sin(\alpha_i)$,

BERLAND ET AL. 11 of 25

2335/084, 2023, 11, Downloaded from https://agupubs.onlinelibrary.wiley.com/doi/10.1029/2023EA002987, Wiley Online Library on [20/08/2024]. See the Terms and Conditions (https://onlinelibrary.wiley.com/terms-and-conditions) on Wiley Online Library for rules of use; OA articles

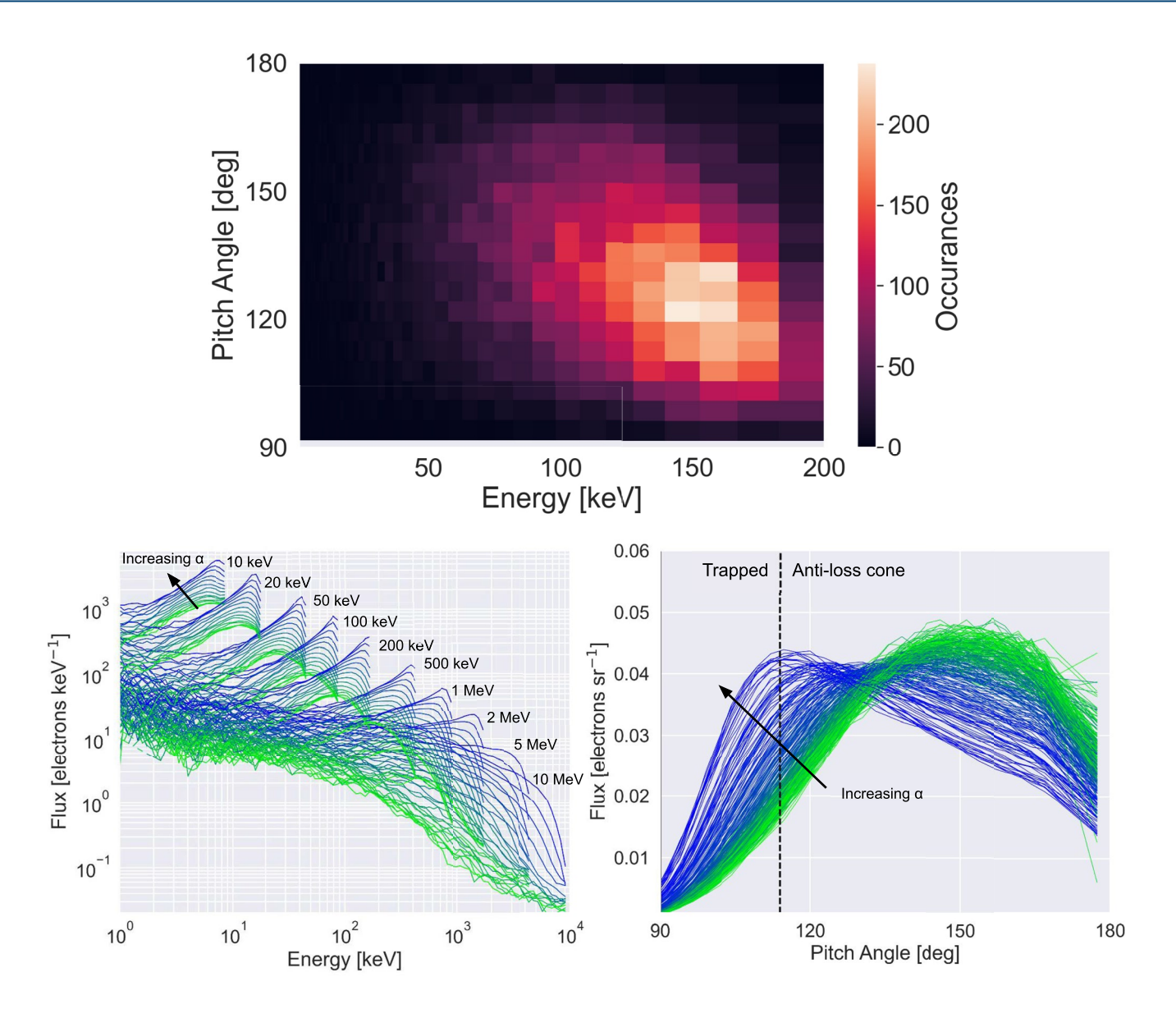


Figure 7. (Top) An example of the coupled energy-pitch angle distribution recorded at 500 km that is output from the model. This distribution comes from an input energy of 200 keV and input pitch angle of 50°. (Bottom) Profiles that are integrated (left) through initial pitch angle to show backscattered electron energy spectra per input pitch angle and beam energy, and (right) integrated through input beam energy to show pitch angle distributions of backscattered electron per input pitch angle. These spectra are recorded at 500 km altitude and are dominated by the primary beam energy with a long tail toward lower energies.

that allows for coupling between energy and pitch angle. We can then write the quantity of interest solution using the set of intensities $S_{ij} \in \mathcal{R}^{N \times M}$:

$$u(E_{\gamma}) = \sum_{i=1}^{N} \sum_{j=1}^{M} S_{ij} \ G(E_i, \alpha_j, E_{\gamma})$$
 (10)

The beam intensities S_{ij} , which are defined on $[0, \infty)$, can be found through a variety of fitting methods; for X-ray spectrum fitting a logarithmic least squares minimization works well in test cases. The formulation for this process is to fit the maximum likelihood spectrum $u_{ML}(E_{\gamma,k})$ to data $g(E_{\gamma,k})$ at each energy bin k and then sum the logarithmic least squares cost function

$$S_{ij}^{ML} = \arg\min_{S_{ij}} \sum_{k} w_k (\log u(E_{\gamma,k}) - \log g(E_{\gamma,k}))^2 = \arg\min_{S_{ij}} \sum_{k} w_k \left(\log \left(\frac{u(E_{\gamma,k})}{g(E_{\gamma,k})} \right) \right)^2$$
(11)

BERLAND ET AL. 12 of 25

23335084, 2023, 11, Downloaded from https://agupubs.onlinelibrary.wiley.com/doi/10.1029/2023EA002987, Wiley Online Library on [20/08/2024]. See the Terms

and-conditions) on Wiley Online Library for rules of use; OA articles are governed by the applicable Creative C

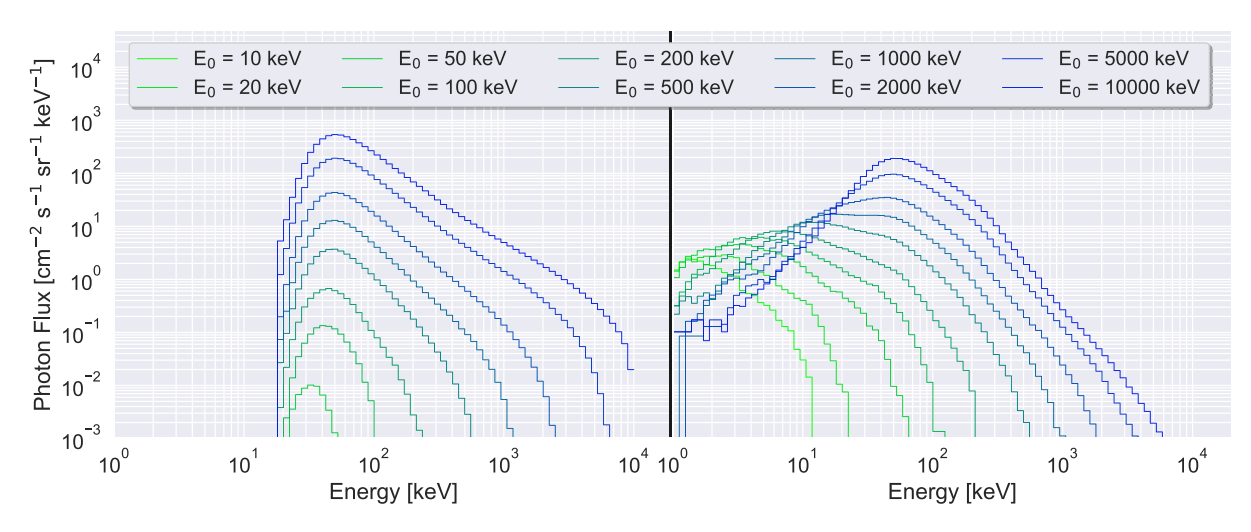


Figure 8. X-ray spectra generated from Geant4 model runs, (left) averaged from 25–35 km and (right) 250–300 km with isotropic pitch angle and mono energy beams with energy E_0 . The energy of peak flux and slope of the tail increase with increasing E_0 . Note that beam energies of 10 and 20 keV are absent from the left plot since those electron energies do not generate X-rays that reach 25–35 km altitude.

where w_k are optional weights for each data point and $u(E_\gamma)$ is generated iteratively through Equation 10. The maximum likelihood Green's function coefficient matrix S_{ij}^{ML} is ultimately found via the Limited-memory Broyden–Fletcher–Goldfarb–Shanno (L-BFGS) global minimization algorithm, which can be run on a personal laptop and allows for a large number of spectral Green's functions to be used (Dai, 2002). The logarithm cost function better emphasizes the smaller numbers in the high energy tail of the X-ray distribution than a linear least squares cost function. The high energy X-ray component is proportional to the high energy electron component, which is important since the highest energy electrons penetrate deepest into the atmosphere and cause X-ray production and ionization at the lowest altitudes.

An example of the latter portion of the Green's function method is shown in Figure 9 where an exponential energy distribution with folding energy $E_0 = 100$ keV and sine pitch angle distribution are recreated using the Green's function coefficient matrix S_{ij} . Slices of the normalized X-ray spectrum for three altitudes are also plotted, illustrating- for the same precipitation event- the range of photon spectra that is measurable. The inversion portion of this method is shown in the case studies in Section 6.

Using this same method, an ionization spectrum versus altitude can be generated from forward modeling loss cone data with linear combinations of the Green's function for ionization at a single energy and pitch angle. In

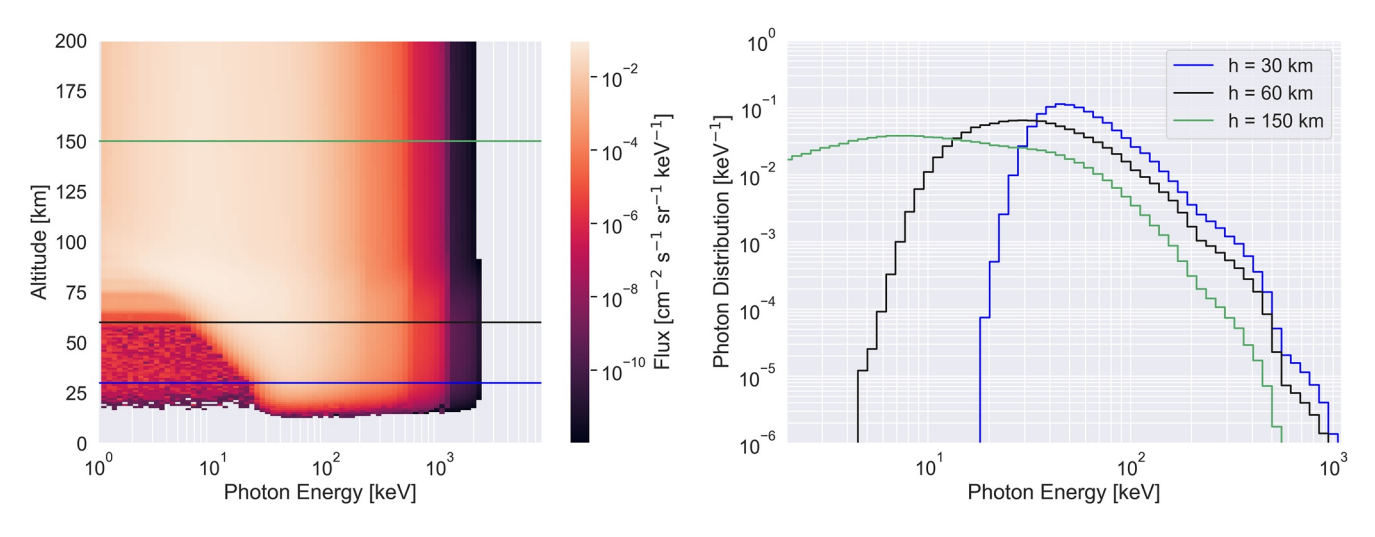


Figure 9. (Left) Photon altitudinal spectra for a precipitation event with differential flux 10^5 cm⁻² s⁻¹ sr⁻¹ keV⁻¹ and exponential energy distribution with folding energy $E_0 = 100$ keV. Note the low flux bins in the lower left-hand corner are from noise. (Right) X-ray spectra averaged at altitudes 30, 60, and 150 km, averaged over a ± 5 km altitude bin.

BERLAND ET AL. 13 of 25



theory, any observable generated by this model can be used to estimate precipitation parameters, however some observables contain less information than others. For instance, X-ray observations are not particularly sensitive to pitch angle. For a further analysis of precipitation inversion via X-ray observations, see Patrick (2022). A 2D fitting process is performed in Section 6.3 using spacecraft 2D electron-pitch angle data at 500 km altitude.

Since we are using a finite number of beams $N \times M$, a degree of uncertainty is introduced in the reconstruction of the forcing function $f(E, \alpha)$. Instead of Dirac delta functions, we can let our EPP forcing spectrum be an arbitrary smooth function, or combination of smooth functions, that we can use in the inversion problem. Xu and Marshall (2019) and Patrick (2022) show the extent of successful reproduction of various forcing distributions using mono-energetic beams. Various other choices of EPP forcing function include a single exponential distribution, or sum of exponential distributions characterized by folding energies, or power law distributions characterized by spectral coefficients. Studies of these distributions are left to future work since there is a dearth of coincident X-ray and in-situ electron measurements that are needed to validate the use of different spectral distributions. Interestingly, an example of a successful inversion using X-ray and electron data has been performed at Jupiter in the work of Mori et al. (2022).

6. Model Validation Through Case Studies

We aim to verify that the model results are quantitatively accurate and are not dissimilar from the previous model of Xu et al. (2020). The authors of Xu et al. (2020) compare their work with the previous model of Fang et al. (2008, 2010), which in turn compares to the older, purely analytical model of R. Roble and Ridley (1987) so the progression of model accuracy can be discerned.

In addition to a comparison with previous work, we aim to validate the model observables and inversion methods using electron and photon measurements, both in situ and remotely sensed. In this section we present two case studies. The first case study analyzes X-ray spectra measured by the BARREL balloon campaigns while the FIREBIRD spacecraft was in magnetic conjunction to measure the electron spectrum in situ. The second case study uses electron energy-pitch angle measurements from the Electron Loss and Fields Investigation with a Spatio-Temporal Ambiguity-Resolving (ELFIN) CubeSat missions to forward and inverse model atmospheric ionization.

6.1. Comparison With Previous Models

Figure 10 shows the difference in ionization profile between this work and the results of Xu et al. (2020), which do not include photon and subsequent secondary electron transport to lower altitudes. For this study, the same reference atmosphere and input space are used to compare the two models. Geant4 predicts lower altitudes of maximum ionization than Energetic Particle Monte Carlo (EPMC) at beam energies less than 50 keV and higher peak altitudes at higher beam energies. Notably, the bremsstrahlung secondary peak extends much further downwards in altitude than the primary ionization peak but is generally two orders of magnitude lower in deposited energy, which may be an important effect in radiation dose at airline altitudes (Tobiska et al., 2016, 2022).

Figure 11 shows a comparison between EPMC simulation results from Xu et al. (2018), where photon transport is handled by a separate model, and the Geant4 simulations across a larger range of energies at two discrete pitch angles. A peak that is both higher and more narrow in altitude is seen in the Geant4 results, in addition to more ionization below the main peak from photon and secondary electron transport. For higher energy electrons beams, the EPMC and Geant4 results match more closely in the secondary peak. This matches with the prediction in Köhn and Ebert (2014) which states the EPMC regime of bremsstrahlung cross section validity is $\hbar\omega \ll E_e$. This approximation in the EPMC implementation should mainly affect the lower, secondary ionization peaks, and the specific ways in which the cross section deviates from a more accurate bremsstrahlung cross section is described by Köhn and Ebert (2014).

6.2. X-Ray Production in the Stratosphere

The goal of this case study is to analyze a time window in which X-ray data measured from within the atmosphere and in situ electron spectra are detected from above the atmosphere during the same precipitation event in a reanalysis of B. Anderson et al. (2017) using the results of this work as an atmospheric forward model. In this

BERLAND ET AL. 14 of 25

2335084, 2023, 11, Downloaded from https://agupubs.onlinelibrary.wiley.com/doi/10.1029/2023EA002987, Wiley Online Library on [20/08/2024]. See the Terms and Conditions (https://online

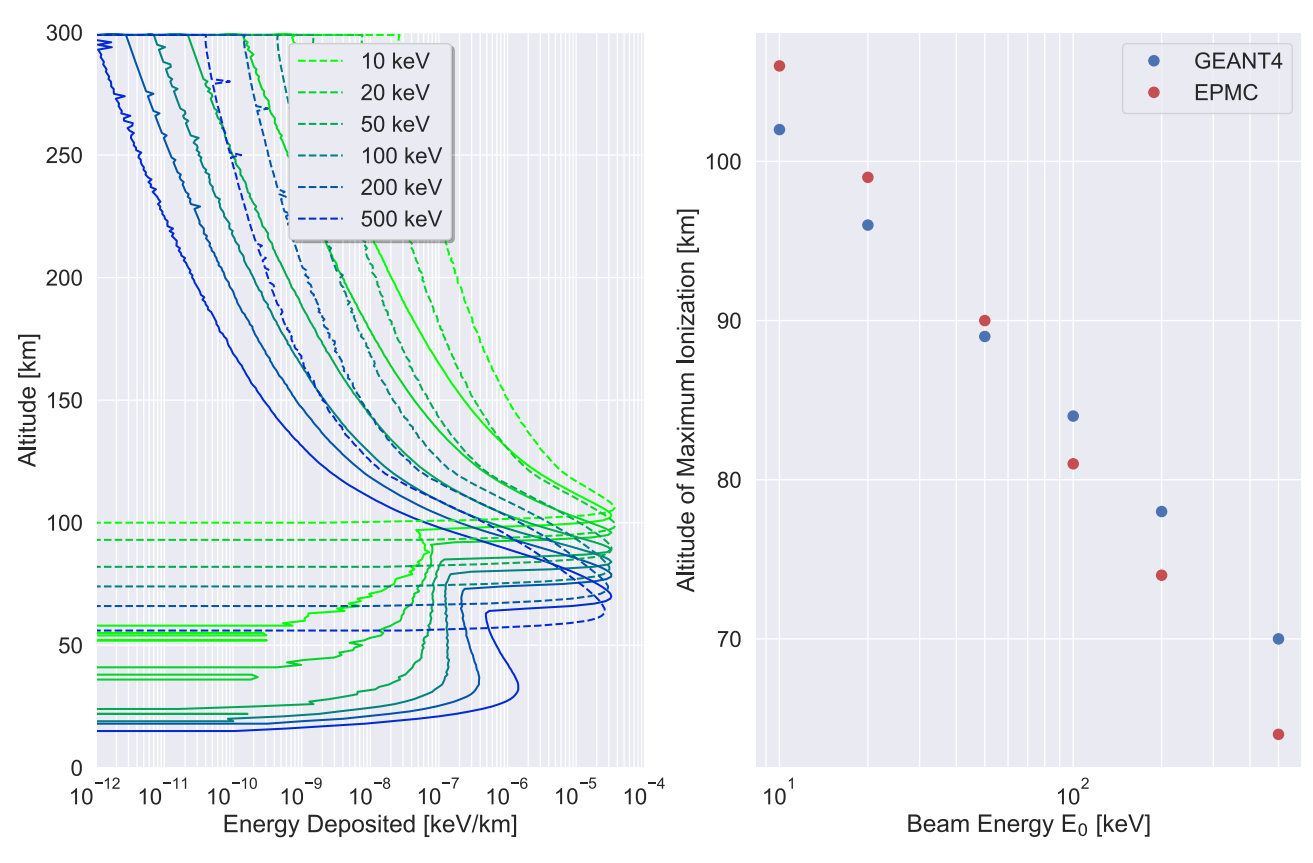


Figure 10. (Left) Geant4 (solid lines) and Energetic Particle Monte Carlo code (Xu et al., 2020) (dashed lines) normalized energy deposition profiles with an isotropic pitch angle distribution at six energies up to 500 keV. (Right) Altitude of the maximum ionization peak with electron beam energy.

study, the EPP phenomenon is specifically microburst precipitation, which is associated with high energy precipitation on small spatial and temporal scales which may have a significant impact on the atmosphere (Seppälä et al., 2018; Shumko et al., 2018; Zhang et al., 2022). Additionally, microburst precipitation is associated with a slowly varying (5–15 s period) X-ray signal that has been measured from balloon and rocket X-ray payloads (Tsurutani et al., 2013). In this study, balloon X-ray measurements are made from the BARREL mission and in-situ electron measurements from the FIREBIRD-II CubeSat mission.

The BARREL missions were a series of stratospheric balloon flights in Antarctica and Sweden that achieved altitudes of >30 km for extended periods of time to study X-ray production from EPP with an upwards (vertical) look direction (Millan et al., 2013). The balloon launches overlap with the Van Allen Probes era, although conjunction data are not always available depending on the location of the Van Allen Probes spacecraft along their orbits (Fox & Burch, 2014). The payloads were sodium iodide (NaI) scintillators with 256 energy channels ranging from 20 keV–10 MeV with an energy-dependent geometric factor. Data from 13 August 2015 from B. Anderson et al. (2017) is selected when the balloon is at approximately L=6.

FIREBIRD-II was a pair of 1.5 U ("unit," where 1 $U = 10^3$ cm³) CubeSats at a close spatial separation which aimed to determine the scale sizes of precipitation regions. They each had two detectors: a surface detector with a nearly 2π sr field-of-view and a collimated detector with an approximately 45° field-of-view (Crew et al., 2016; Johnson et al., 2020). The electron data reported in B. Anderson et al. (2017) is in counts per energy channel, so the energy-dependent geometric factors from Johnson et al. (2020) are used to convert counts to physical flux units, then an estimate of the electron flux and spectrum at various times in the conjunction are made and are shown in Figure 14. The FIREBIRD satellite had a "wobble" period that is described in B. Anderson et al. (2017) that implies the detectors were sampling portions of the trapped, loss cone, and anti-loss cone populations. For this reason, the surface detector is taken as the more consistent measurement of flux as the larger field-of-view measurement should vary less in angular coverage of trapped versus non-trapped electrons than the collimated detector, given the spacecraft's changing look direction. However, for the same reason, the omni-directional

BERLAND ET AL. 15 of 25

23335084, 2023, 11, Downloaded from https://agupubs.onlinelibrary.wiley.com/doi/10.10292023EA002987, Wiley Online Library on [20/08/2024]. See the Terms and Conditions (https://onlinelibrary.wiley.com/terms-and-conditions) on Wiley Online Library for rules of use; OA articles are governed by the applicable

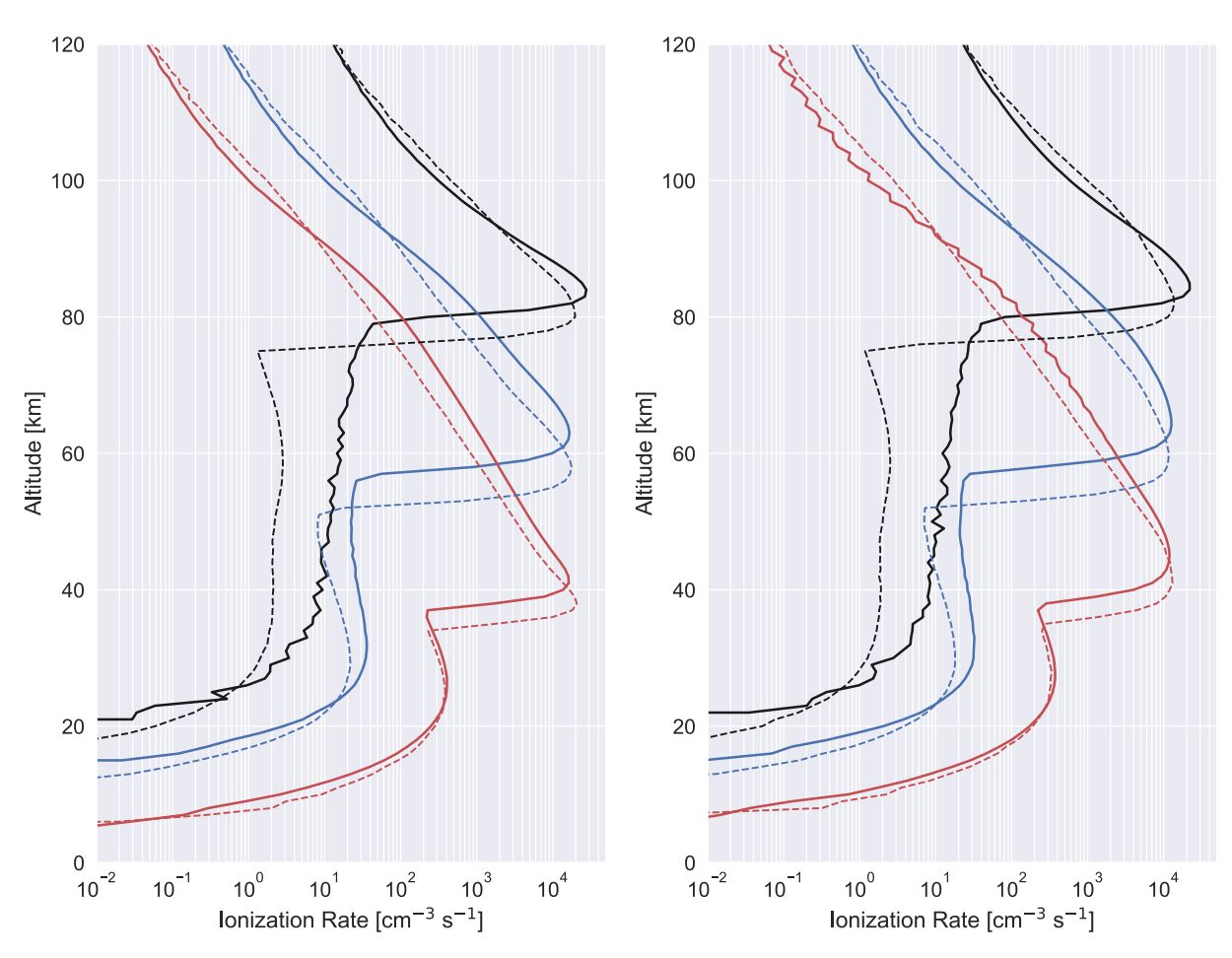


Figure 11. Comparison between ionization profiles generated by Xu et al. (2018) (dashed lines) and the Geant4 model presented in this work (solid lines), both of which include photon tracking to lower altitudes. (Left) Simulation run at 0° pitch angle, and (right) 45° pitch angle for energies 100 keV (black), 1 MeV (blue), and 10 MeV (red).

surface detector was subject to more background noise than the collimated detector: the energy-averaged ratio of geometric factors between the surface and collimated detectors is 2.6, while measurements reflect a factor of $10\times$ more counts in the surface detector than the collimated detector. Additionally, FIREBIRD was spatially separated from the magnetic footprint where BARREL detected X-rays. For these reasons, we only use the measured electron spectra as a reference for the electron spectra produced by the X-ray inversion method and not as a target of the fitting procedure. Using the Green's function inversion method, the electron spectrum is estimated via 2-parameter distribution (one spectral shape parameter and one integrated flux scaling parameter) fits to the X-ray data.

The inversion method described in Section 5 requires physical flux units in place of instrument counts, so the following actions were taken to infer the BARREL instrument response to X-rays. An energy-agnostic geometric factor is calculated from the surface area of the 3 inch tall \times 3 inch diameter NaI scintillator crystal, excluding the bottom light-collecting surface, and multiplied by π sr field-of-view which results in a geometric factor of 716 cm² sr (B. Anderson et al., 2017). This geometric factor over-estimates X-ray flux at both high and low energies due to X-ray absorption in the housing material at low energies and the diminishing photon-matter interaction probability at high X-ray energies. At low energies, these regions are outside the lower end of the fitting range, and at high energies, the measurement is dominated by background counts, so these effects are less substantial on the inversion accuracy versus other systemic factors, for example, measurement uncertainty. The processed measurement for the earlier of the two microburst events described in B. Anderson et al. (2017) at 07:55:47 UT is shown in Figure 12 relative to the atmospheric background model.

The background model is an empirically derived spectrum from a survey of BARREL observations that represents the average atmospheric contribution to X-ray measurements. A variety of line transition and other spectral

BERLAND ET AL. 16 of 25

23335084, 2023, 11, Downloaded from https://agupubs.sonlinelibrary.wiley.com/doi/10.1029/2023EA002987, Wiley Online Library on [20/08/204]. See the Terms and Conditions (https://onlinelibrary.wiley.com/terms-and-conditions) on Wiley Online Library for rules of use; OA articles are governed by the applicable Creative C.

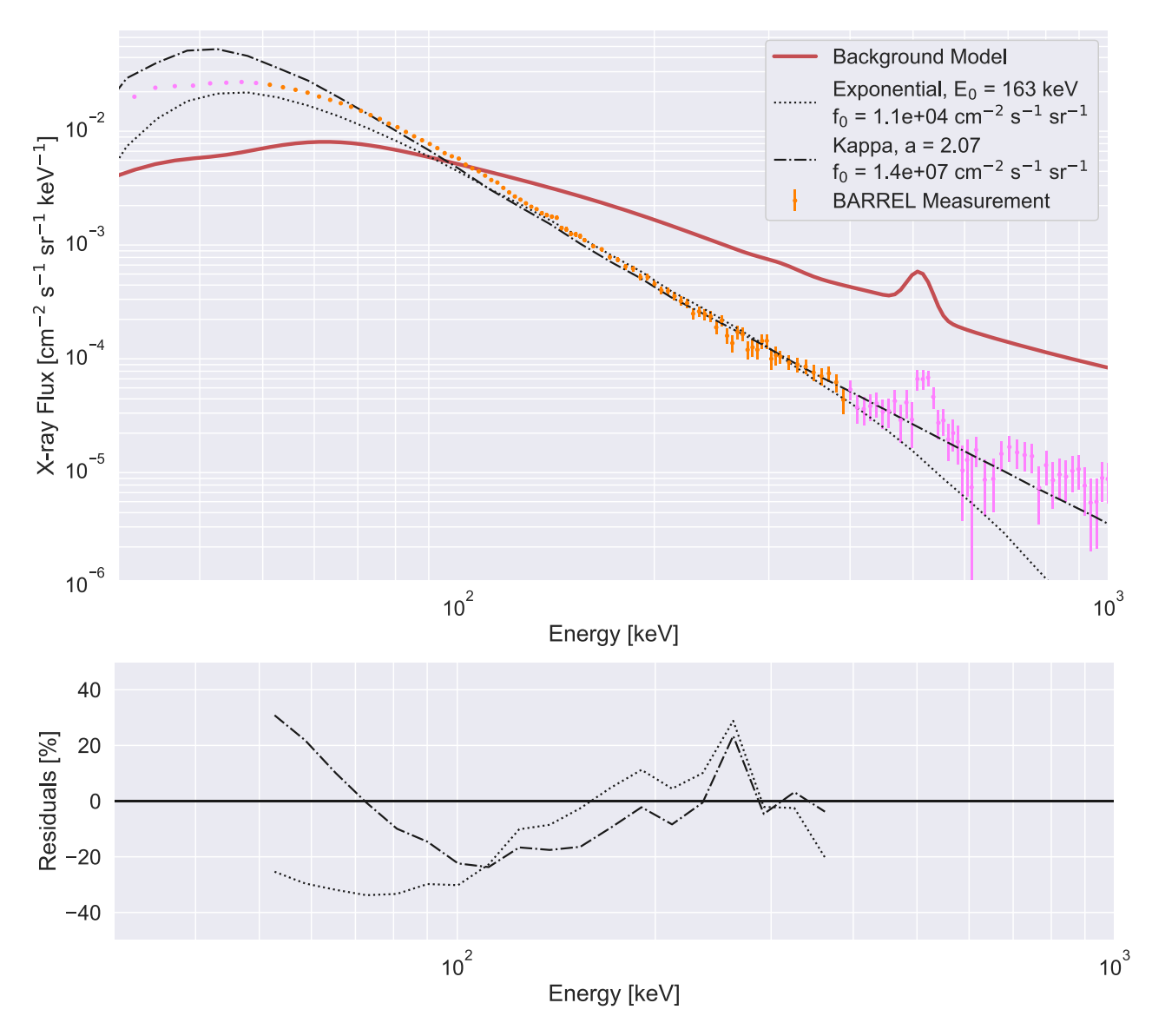


Figure 12. (Top) Balloon Array for RBSP Relativistic Electron Losses (BARREL) background-subtracted X-ray differential flux are shown as orange and purple dots in relation to the atmospheric background model which is shown as a solid red line. These points show measurement uncertainty with bars and the points in orange indicate the portion of the X-ray spectrum used in the inversion process. The black dashed and dotted lines correspond to the X-ray spectra generated by a kappa and exponential energy distribution of precipitating electrons, respectively. (Bottom) The residuals between the Geant4 X-ray spectrum and background model versus the BARREL measurements within the fitting region of 50–400 keV.

peaks are included in the background model using Gaussian functions with the most prominent being the 511 keV annihilation line. Ultimately, the background model is subtracted from the BARREL count data in order to examine the contribution from EPP. The background model is plotted in Figure 12 as a red line along with the background-subtracted BARREL counts at points.

The log-least squares cost function from Equation 11 is employed over a parameter space of (α, f_0) for a 1-parameter kappa distribution of the form

$$f(E) = f_0 \ \alpha(\alpha + E^{\alpha})^{-(\alpha+1)/\alpha} \tag{12}$$

where α is the shape parameter. The parameter space for exponential distributions is (E_0, f_0) for energy distributions of the form

$$f(E) = f_0 \frac{1}{E_0} e^{-E/E_0}$$
 (13)

BERLAND ET AL. 17 of 25

23335084, 2023, 11, Downloaded from https://agupubs.onlinelibrary.wiley.com/doi/10.1029/2023EA002987, Wiley Online Library on [20/08/2024]. See the Terms and Conditi 2335084, 2023, 11, Downloaded from https://agupubs.onlinelibrary.wiley.com/doi/10.1029/2023EA002987, Wiley Online Library on [20/08/2024]. See the Terms and Conditi

articles are governed by the applicable Creative C

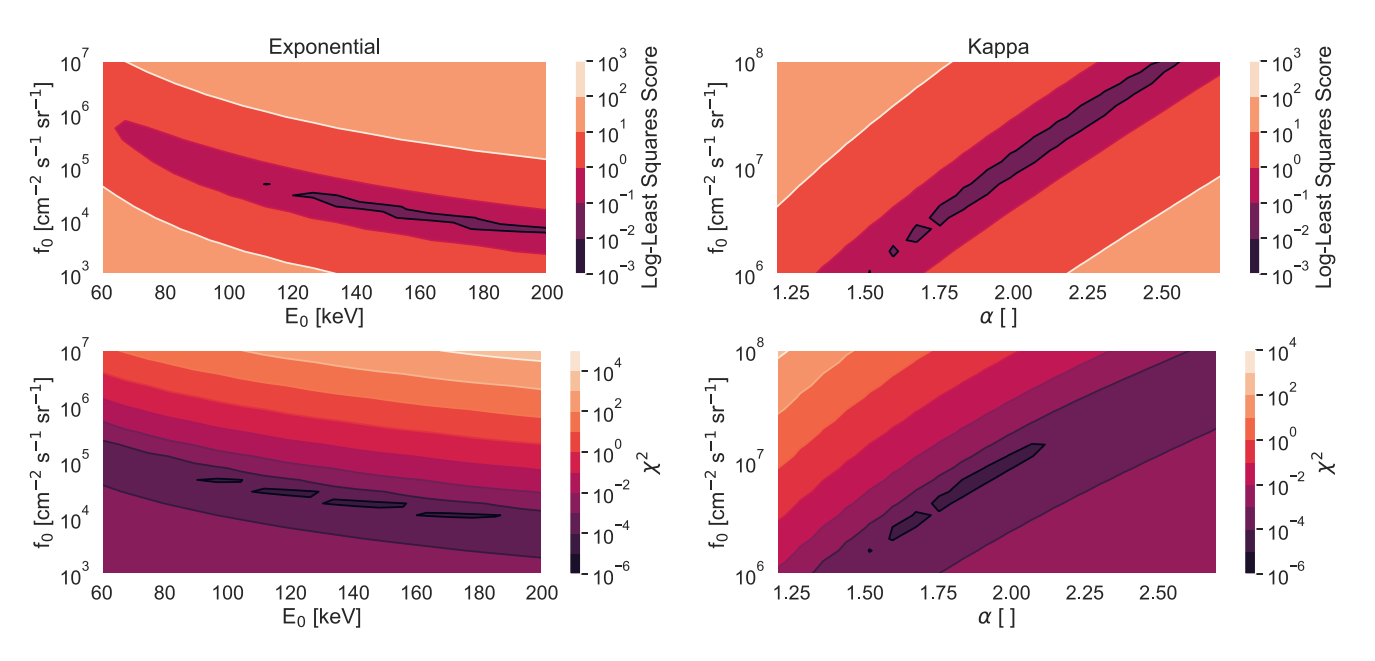


Figure 13. (Top row) The weighted log-least squares cost function evaluation score for the parameter space of (α, f_0) and (E_0, f_0) for kappa and exponential energy distributions, respectively. The regime of minima indicate equally likely inversion spectra estimates within the fitting regime shown in Figure 12. (Bottom row) The same parameter space scored with a χ^2 cost function over the 19 points within the X-ray spectrum fitting region.

where E_0 is the folding energy of the spectrum, and for both equations f_0 is the energy-integrated electron flux. The weights for the cost function are inversely proportional to the measurement uncertainty shown in Figure 12 and normalized to unity. Within the fitting region of 50–400 keV both proposal precipitation spectra show a high degree of agreement but vary substantially outside of the fitting region. Qualitatively speaking, a similar X-ray spectrum can be generated by a high flux of medium energy electrons or low flux of high energy electrons, which leads to ambiguity between the electron flux and characteristic energy parameter based on the choice of input energy distribution and highlights the non-uniqueness of this inversion problem.

The resulting score of the log-least squares minimization grid search is shown in the top row of Figure 13, above the χ^2 score for the same parameters in the bottom row for reference. The electron distribution parameter sets that realistically reproduce the X-ray spectrum shown in Figure 12 exhibit an approximately linear relationship between the two-parameter fits in semi-log space. The range of parameters that represent the minima of the electron spectral distribution spaces are within the range $\alpha \in [1.67, 2.46]$ and $f_0 \in [1.77 \times 10^6, 8.42 \times 10^7]$ cm⁻² s⁻¹ sr⁻¹ for the kappa distribution and $E_0 \in [110, 200]$ keV and $f_0 \in [4.4 \times 10^3, 4 \times 10^4]$ cm⁻² s⁻¹sr⁻¹ for the exponential distribution. The valleys of cost score minima shown in Figure 13 create a manifold of potential precipitating electron spectra, that, without further constraints, are equally likely to have caused the observed X-ray spectra in a maximum likelihood sense. The 1-parameter kappa distribution performs similarly well in the inversion process to a power law distribution of the form $E^{-\Gamma}$ with spectral index Γ . The range of electron spectra that satisfy the cost function minima are plotted with a finite resolution over FIREBIRD measurements in Figure 14.

From comparing the range of realistic electron spectral inversion estimates to in situ electron measurements, the Geant4 X-ray production and transport modeling is validated, and the inversion process viable. Future work toward a higher-confidence inversion of balloon-measured X-ray spectra to precipitating electron spectra may be possible by analyzing events with a more significant detection of the X-ray high-energy tail and by including more uncertainty modeling, for example, the background model uncertainty. Further, by propagating measurement, background, and X-ray generation and transport uncertainties through the inversion process, spectral error bars can be included in this analysis.

6.3. Atmospheric Backscatter of Radiation Belt Electrons

In this case study, we consider the population of energetic electrons that are backscattered by the atmosphere, which is an observable quantity from this model. This population includes the case of electrons that have pitch

BERLAND ET AL. 18 of 25

2333584, 2023, 11, Downloaded from https://agupub.son/inclibrary.wiley.com/doi/10.1029/2023EA002987, Wiley Online Library on [20/08/2024]. See the Terms and Conditions (https://onlinelibrary.wiley.com/terms-and-conditions) on Wiley Online Library for rules of use; OA articles are governed by the applicable Creative Commons Liceasure C

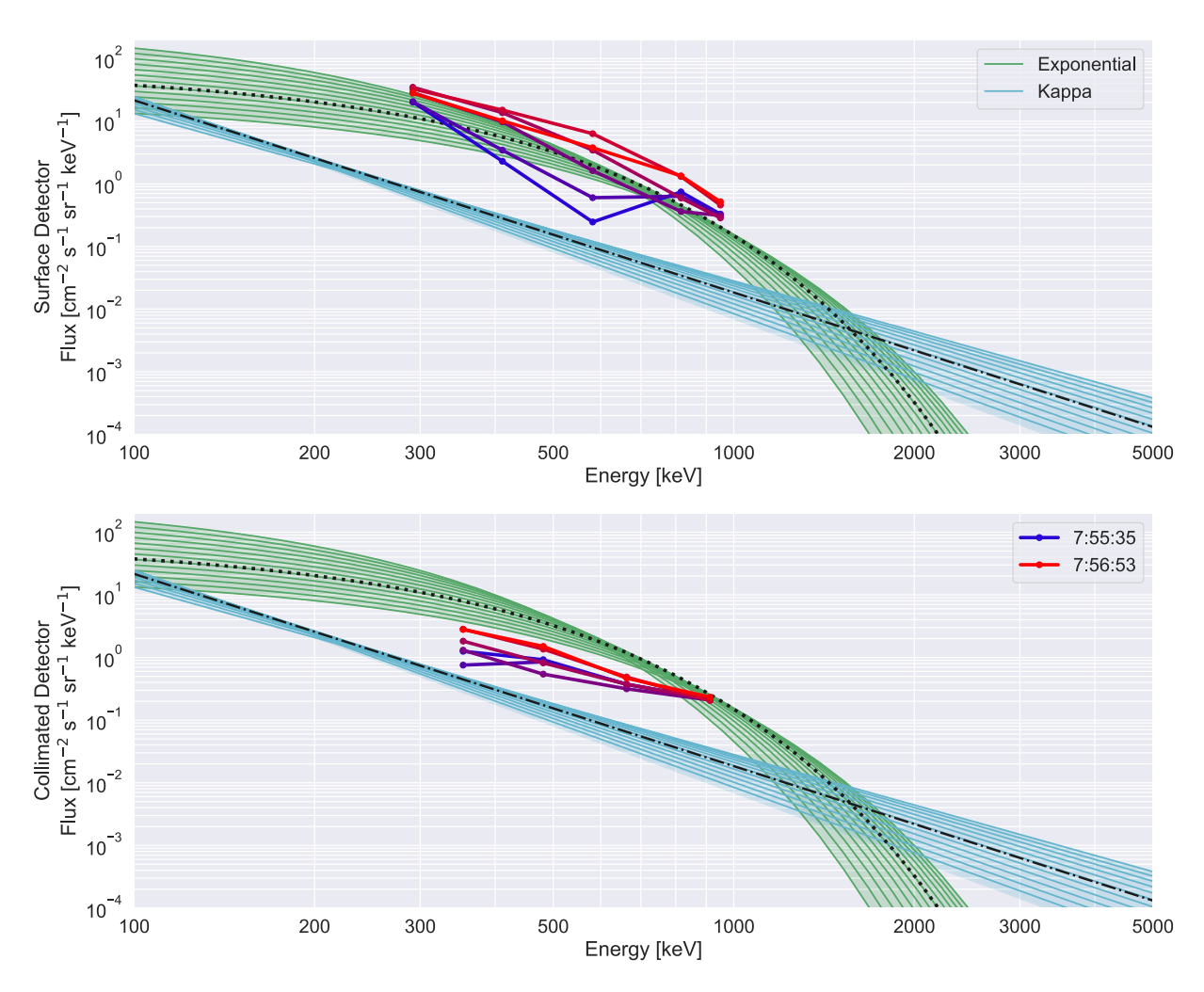


Figure 14. In situ electron measurements from the FIREBIRD 180°-FOV surface detector (top plot) and 45°-FOV collimated detector (bottom plot) electron spectra during the approximate conjunction between FIREBIRD and Balloon Array for RBSP Relativistic Electron Losses, where earlier spectra are in blue and progress to red. The spectra are averaged over 13 s windows, and the first two channels of each FIREBIRD detector are removed due to noise. The light blue region shows the regime of viable electron kappa distributions and the green shows viable exponential energy distributions. The black lines indicate the electron spectra that generated the corresponding style line X-ray spectra in Figure 12.

angles within the loss cone but ultimately are not lost to the atmosphere, as well as the case of secondary electron production in the upper atmosphere where those newly produced electrons rejoin the free electrons in the radiation belts undergoing cyclotron motion. The former process can occur through electron-neutral pitch angle scattering that reverses the field-aligned component of an electron's momentum vector, and the latter case can occur from impact ionization in which the secondary electron's momentum vector is anti-Earthwards. These two populations are separate in origin, but to a low-Earth orbit (LEO) spacecraft may be indistinguishable in measurement. This process has wide reaching implications for magnetosphere-ionosphere coupling and the generation of diffuse aurora, atmospheric electrodynamics, and electron lifetime calculations (Khazanov & Chen, 2021; Marshall & Bortnik, 2018; Selesnick et al., 2004).

The Geant4 model predicts a certain amount of electron backscatter per injected electron beam for a given input energy and pitch angle. We seek to validate that these model results accurately describe the electron backscatter phenomenon with in-situ electron data. Selected for this study is the ELFIN mission: a pair of CubeSats that spin in order to measure the full pitch angle distribution of electrons from 63 keV–6 MeV in a LEO orbit of 450 km altitude (Angelopoulos et al., 2020). These data are well suited to estimate both precipitating electrons in the loss cone as well as backscattered electrons in the anti-loss cone.

BERLAND ET AL. 19 of 25

2335/864, 2023, 11, Downloaded from https://agupubs.on/inelibrary.wiley.com/doi/10.1029/2023EA002987, Wiley Online Library on [20/08/2024]. See the Terms and Conditions (https://onlinelibrary.wiley.com/terms-and-conditions) on Wiley Online Library for rules of use; OA articles are governed by the applicable Creative Commons Licenses

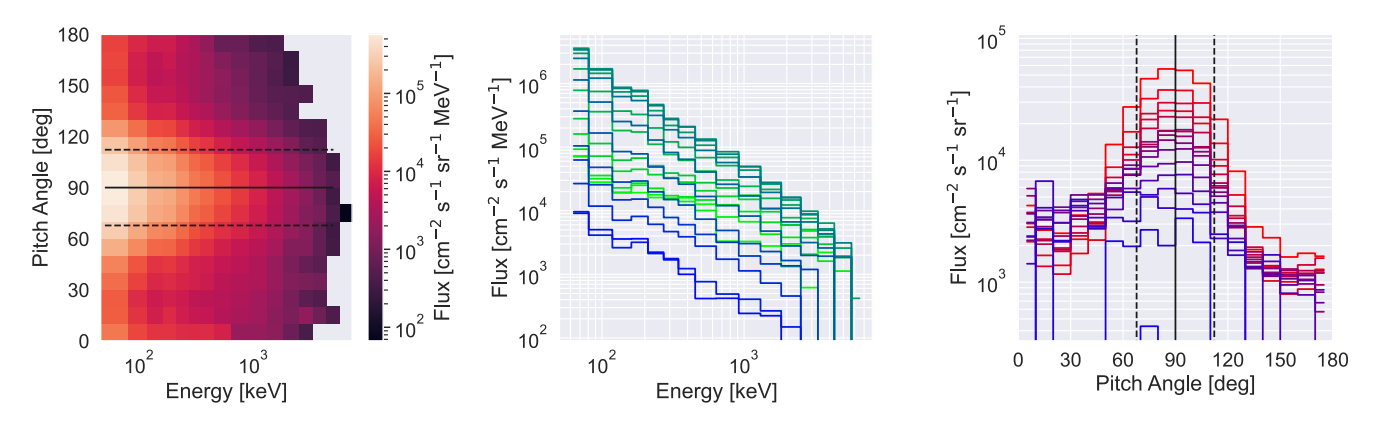


Figure 15. (Left) Electron Loss and Fields Investigation with a Spatio-Temporal Ambiguity-Resolving 2D energy-pitch angle data averaged over 144 events during electromagnetic ion cyclotron wave-driven precipitation measured at 500 km altitude. (Center) Integration of the 2D data over the pitch angle dimension to show energy spectra per pitch angle bin using 10° pitch angle bin sizes. Light green denotes pitch angles within the loss cone, dark green are trapped population angles, and blue are anti-loss cone pitch angles. (Right) Integration of the 2D data over the energy dimension to show pitch angle distribution per energy bin. Red are lower energy bins and blue are higher energy bins. The dashed lines represent the edges of the loss cone and anti-loss cone, respectively, and the solid line is at 90°.

In this section, we use the ability of ELFIN to directly measure backscattered electrons to validate the Geant4 model. We use the energy and pitch-angle distributions in the public catalog of precipitation events likely associated with electromagnetic ion cyclotron (EMIC) waves, provided by Capannolo et al. (under review 2023). Electromagnetic ion cyclotron waves preferentially precipitate ~MeV energy electrons into the Earth's atmos-

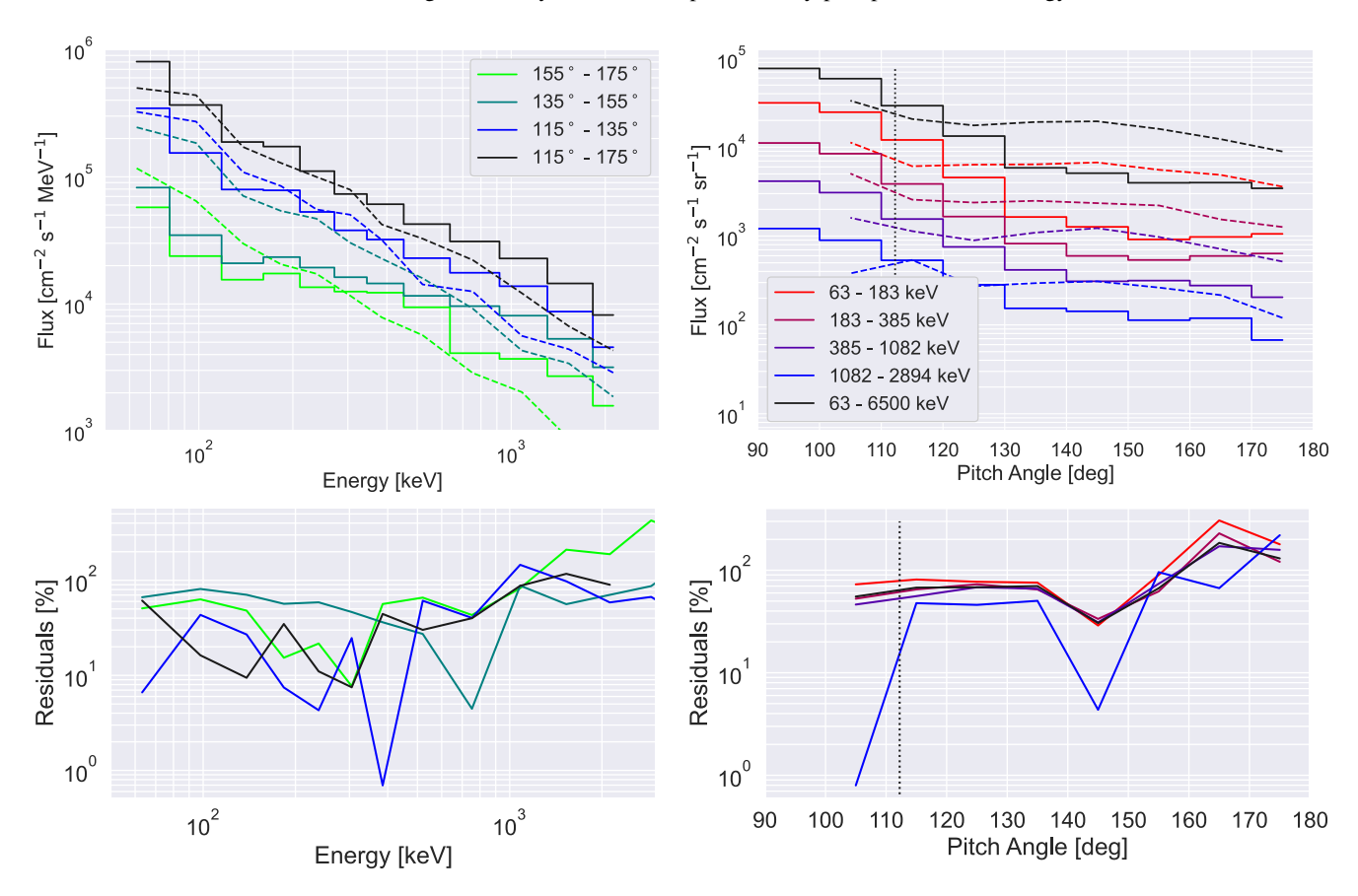


Figure 16. The top row shows the anti-loss cone portion of the 144 event-averaged Electron Loss and Fields Investigation with a Spatio-Temporal Ambiguity-Resolving data from Figure 15 (solid lines) and a 2D surface fit (dashed lines) to the data, where the left plot is an integration of the 2D data over pitch angle to show the energy spectra and the right plot is an integration over the energy dimension to show pitch angle distributions. The various series in the left plot are using 20° bin sizes and the black line is the integral over the entire pitch angle dimension. Similarly, the right plot shows varying energy bin size and the black line is the integral over the entire energy range. The bottom row of plots show the residuals between the data and the surface fit per data series.

BERLAND ET AL. 20 of 25

23335084, 2023, 11, Downloaded from https:/

viley.com/doi/10.1029/2023EA002987, Wiley Online Library on [20/08/2024]. See the Terms

phere and are also associated with strong proton precipitation (Blum et al., 2020; Carson et al., 2013; Capannolo, Li, Ma, Chen, et al., 2019; Capannolo, Li, Ma, Shen, et al., 2019). Within the scope of this work, the exact wave driver of the precipitation is not essential; however, the Capannolo et al. (under review 2023) catalog is public and events have been carefully selected to avoid possible instrumentation errors and are processed to remove noise (e.g., from low electron counts). More details on the analysis can be found in Capannolo et al. (under review 2023). For our validation case study, we use data averaged over 144 ELFIN events that were recorded during EMIC wave-driven precipitation activity. Figure 15 shows the average 2D pitch angle-spectra measurement from ELFIN, which is in differential flux units of cm⁻² s⁻¹ sr⁻¹ MeV⁻¹. The data is configured such that the bounce loss cone is between 0°–66°, 114°–180° is the anti-bounce loss cone, and between those angular ranges are the trapped population of electrons.

Two methods are employed in this analysis, both of which are ultimately used to estimate atmospheric ionization profiles, which are a vital output of this model for atmospheric modeling: the first involves inverting the ELFIN-measured anti-loss cone distribution and the second involves forward-modeling the ELFIN-measured loss cone distribution. To generate ionization profiles from these two methods, the total input energy flux is calculated from either the loss cone flux data directly or from the inversion estimate of loss cone flux, then used as a constraint on the total integrated ionization. An integral over solid angle and energy of the measurement provides the total precipitating energy flux

$$\int_{E_{low}}^{E_{high}} \int_{0}^{\alpha_{LC}} f(E, \alpha) \cdot E \sin(\alpha) \ d\alpha \ dE$$
 (14)

where $f(E, \alpha)$ are the spectral-pitch angle data, E_{low} and E_{high} are the lowest and highest energy bins, respectively, and α_{LC} is the angular extent of the loss cone, which is 66° on average at the ELFIN spacecraft altitude. This integral returns the input energy flux to the model in units of eV cm⁻² s⁻¹, which is divided by 35 eV cm pair⁻¹ (described in Section 3) to obtain ionization rate in units of pairs cm⁻³ s⁻¹.

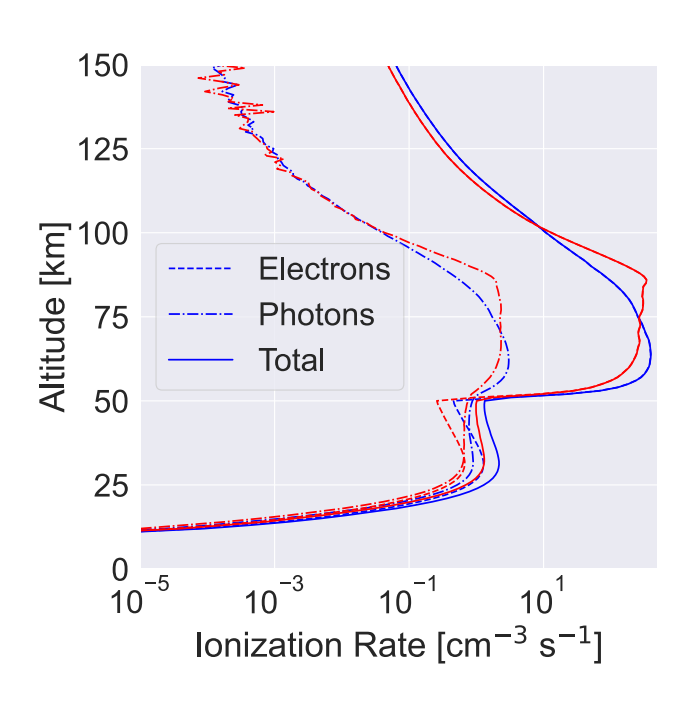


Figure 17. Predicted atmospheric ionization response from Electron Loss and Fields Investigation with a Spatio-Temporal Ambiguity-Resolving data, performed with the methods described in Section 6.3: method 1 (blue) fits a surface to backscattered electron data and inverts to ionization profile, and method 2 (red) directly forward models loss cone data. The dotted lines shows the ionization rates caused by electron ionization, the dash-dotted line shows corresponds to photoionization, and the solid line is the sum of the two.

The inversion method is performed by fitting a surface to the electron backscatter spectrum and recording the Green's function coefficients used to generate that surface. From there, a linear combination of the electron input space (E_0, α_0) is formed with the coefficients acting as weights. The same weights are applied to the Green's function ionization profiles and normalized by the loss cone input energy flux to ensure the correct amount of column-integrated ionization. The results of the 2D surface fit and the residuals are shown in Figure 16. The surface fit is biased to better capture the behavior of the energy dimension of the 2D data versus the pitch angle dimension since the ionization profile is a strong function of the shape of the input electron spectrum, and is only weakly affected by the pitch angle distribution. This case study is formulated to match the estimated ionization profile generated from the forward and inverse methods, since that is one of the outputs of this modeling effort. The corresponding ionization profile versus altitude generated by this method is shown in blue in Figure 17.

The second method is a direct forward modeling of the ELFIN loss cone data where the data are evaluated at the input control points (E_0, α_0) to generate weights for the linear combination method. The results of the forward modeling are used as a control or "truth" value for this analysis and are shown in red in Figure 17.

We find that the ionization profiles from these two methods match in general shape characteristics, such as the altitude of maximum ionization and the lowest ionization altitude. We conclude that this model can effectively generate ionization profiles using either direct loss cone measurements or backscattered electron measurements, which is an indirect validation of both the backscattered electron data as well as the Green's function inversion method in 2D.

BERLAND ET AL. 21 of 25

2335084, 2023, 11, Downloaded from https://agupubs.onlinelibrary.wiley.com/doi/10.1029/2023EA002987, Wiley Online Library on [20/08/2024]. See the Terms and Conditions (https://

7. G4EPP Software Package

The Python package G4EPP has been developed to allow convenient user access to the data generated by this model, as well as a handful of analysis implementations that were used in this work. The software package is a class-based implementation that allows users to import an application programming interface (API) into their Python program and use the analysis methods directly in their code. Documentation for G4EPP implementation is included in Jupyter Notebooks which provide example usages of the methods, and direct access to the Geant4 data products is offered through the API as well.

Ionization profiles versus altitude can be generated from arbitrary initial energy and pitch angle distributions. Closed-form spectral distributions included in this package are exponential, power law, single and double Maxwellian, and relativistic Maxwellian distributions. These are used are commonly used for radiation belt electron spectral modeling and also have been applied to Polar Operational Environmental Satellites Medium Energy Proton and Electron Detector data. Additionally, the package offers the capability to convert from the reference atmosphere taken at PFISR to various atmospheric profiles via a scaling method implemented in Xu et al. (2020).

8. Conclusions

A new model of EPP has been developed based on the Geant4 particle transport code. This code simulates EPP over a range of input parameters and simulation conditions to produce a lookup table from which measurement-based inversions can be performed to estimate precipitating electron parameters, including energy spectrum and flux. This model offers improvements over previous works, which are compared to these results to verify this work.

The results of this model are validated using balloon X-ray and satellite electron data. Through this analysis, the inversion techniques described are performed and return reasonable and realistic values for EPP parameters. Finally, a Python package is described that allows for user access to these data.

Data Availability Statement

BARREL datacan be accessed at barreldata.ucsc.edu/data_products/and using the SPEDAS software (Angelopoulos et al., 2019). ELFIN data are available at plots.elfin.ucla.edu/. The G4EPP Python software used for EPP analysis in the study are available at github.com/GrantBerland/G4EPP via https://doi.org/10.5281/zenodo.8226181 with the MIT license (Berland, 2023). Documentation and example usage are also at this GitHub link, as well as the BARREL atmospheric background model. The data used for the EPP analysis is automatically downloaded by G4EPP on first use or can be accessed separately at zenodo.org/record/8034275 via https://doi.org/10.22541/essoar.168286498.89947288/v1 with the Creative Commons Attribution 4.0 International license.

Acknowledgments Ref

This work was supported by NASA Grant 80NSSC19K0648 to the University of Colorado Boulder. The authors would like to thank Robyn Millan and the BARREL team for their help in BARREL data retrieval and analysis, and the ELFIN team for operation of the mission and for making the data available. A special thanks to Wei Xu for his mentorship in the many details of EPP modeling. This work utilized the Blanca condo computing resource at the University of Colorado Boulder. Blanca is jointly funded by computing users and the University of Colorado Boulder.

References

- Agostinelli, S., Allison, J., Amako, K. A., Apostolakis, J., Araujo, H., Arce, P., et al. (2003). Geant4—A simulation toolkit. *Nuclear Instruments and Methods in Physics Research Section A: Accelerators, Spectrometers, Detectors and Associated Equipment*, 506(3), 250–303. https://doi.org/10.1016/s0168-9002(03)01368-8
- Akasofu, S.-I., & Chapman, S. (1961). The ring current, geomagnetic disturbance, and the Van Allen radiation belts. *Journal of Geophysical Research*, 66(5), 1321–1350. https://doi.org/10.1029/jz066i005p01321
- Alken, P., Thébault, E., Beggan, C. D., Amit, H., Aubert, J., Baerenzung, J., et al. (2021). International geomagnetic reference field: The thirteenth generation. *Earth Planets and Space*, 73(1), 1–25. https://doi.org/10.1186/s40623-020-01288-x
- Allison, J., Amako, K., Apostolakis, J., Araujo, H., Dubois, P. A., Asai, M., et al. (2006). Geant4 developments and applications. *IEEE Transactions on Nuclear Science*, 53(1), 270–278. https://doi.org/10.1109/tns.2006.869826
- Anderson, B., Shekhar, S., Millan, R., Crew, A., Spence, H., Klumpar, D., et al. (2017). Spatial scale and duration of one microburst region on 13 August 2015. *Journal of Geophysical Research: Space Physics*, 122(6), 5949–5964. https://doi.org/10.1002/2016ja023752
- Anderson, R., Harvey, C. C., Hoppe, M., Tsurutani, B., Eastman, T., & Etcheto, J. (1982). Plasma waves near the magnetopause. *Journal of Geophysical Research*, 87(A4), 2087–2107. https://doi.org/10.1029/ja087ia04p02087
- Andersson, M., Verronen, P., Rodger, C., Clilverd, M., & Seppälä, A. (2014). Missing driver in the Sun–Earth connection from energetic electron precipitation impacts mesospheric ozone. *Nature Communications*, 5(1), 1–5. https://doi.org/10.1038/ncomms6197
- Angelopoulos, V., Cruce, P., Drozdov, A., Grimes, E., Hatzigeorgiu, N., King, D., et al. (2019). The space physics environment data analysis system (SPEDAS). Space Science Reviews, 215, 1–46. https://doi.org/10.1007/s11214-018-0576-4
- Angelopoulos, V., Tsai, E., Bingley, L., Shaffer, C., Turner, D., Runov, A., et al. (2020). The Elfin mission. Space Science Reviews, 216(5), 1–45. https://doi.org/10.1007/s11214-020-00721-7
- Asikainen, T., & Ruopsa, M. (2016). Solar wind drivers of energetic electron precipitation. *Journal of Geophysical Research: Space Physics*, 121(3), 2209–2225. https://doi.org/10.1002/2015ja022215

BERLAND ET AL. 22 of 25

- Baker, D., Erickson, P., Fennell, J., Foster, J., Jaynes, A., & Verronen, P. (2018). Space weather effects in the Earth's radiation belts. *Space Science Reviews*, 214, 1–60. https://doi.org/10.1007/s11214-017-0452-7
- Berger, M., & Seltzer, S. (1972). Bremsstrahlung in the atmosphere. Journal of Atmospheric and Terrestrial Physics, 34(1), 85–108. https://doi.org/10.1016/0021-9169(72)90006-2
- Berger, M., Seltzer, S., & Maeda, K. (1974). Some new results on electron transport in the atmosphere. *Journal of Atmospheric and Terrestrial Physics*, 36(4), 591–617. https://doi.org/10.1016/0021-9169(74)90085-3
- Berland, G. (2023). G4EPP. Retrieved from https://github.com/GrantBerland/G4EPP
- Berland, G., Marshall, R., Martin, C., Buescher, J., Kohnert, R., Boyajian, S., et al. (2023). The atmospheric x-ray imaging spectrometer (AXIS) instrument: Quantifying energetic particle precipitation through bremsstrahlung x-ray imaging. *Review of Scientific Instruments*, 94(2), 023103. https://doi.org/10.1063/5.0127272
- Bhardwaj, A., Elsner, R. F., Gladstone, G. R., Cravens, T. E., Lisse, C. M., Dennerl, K., et al. (2007). X-rays from solar system objects. *Planetary and Space Science*, 55(9), 1135–1189. https://doi.org/10.1016/j.pss.2006.11.009
- Blum, L. W., & Breneman, A. W. (2020). Observations of radiation belt losses due to cyclotron wave-particle interactions. In *The dynamic loss of Earth's radiation belts* (pp. 49–98). Elsevier.
- Blum, L. W., Remya, B., Denton, M., & Schiller, Q. (2020). Persistent emic wave activity across the nightside inner magnetosphere. *Geophysical Research Letters*, 47(6), e2020GL087009. https://doi.org/10.1029/2020gl087009
- Bunkin, F., & Fedorov, M. (1966). Bremsstrahlung in a strong radiation field. Soviet Physics Journal of Experimental and Theoretical Physics,
- Capannolo, L., Li, W., Ma, Q., Chen, L., Shen, X.-C., Spence, H., et al. (2019). Direct observation of subrelativistic electron precipitation potentially driven by emic waves. *Geophysical Research Letters*. 46(22), 12711–12721. https://doi.org/10.1029/2019g1084202
- Capannolo, L., Li, W., Ma, Q., Shen, X.-C., Angelopoulos, V., Artemyev, A., et al. (2023). Electron precipitation observed by elfin using proton precipitation as a proxy for electromagnetic ion cyclotron (EMIC) waves. *Geophysical Research Letters*, 50(8). (under review 2023). https://doi.org/10.1029/2022g1101682
- Capannolo, L., Li, W., Ma, Q., Shen, X.-C., Zhang, X.-J., Redmon, R., et al. (2019). Energetic electron precipitation: Multievent analysis of its spatial extent during emic wave activity. *Journal of Geophysical Research: Space Physics*, 124(4), 2466–2483. https://doi.org/10.1029/2018ja026291
- Capannolo, L., Li, W., Spence, H., Johnson, A., Shumko, M., Sample, J., & Klumpar, D. (2021). Energetic electron precipitation observed by FIREBIRD-II potentially driven by EMIC waves: Location, extent, and energy range from a multievent analysis. *Geophysical Research Letters*, 48(5), e2020GL091564. https://doi.org/10.1029/2020gl091564
- Carson, B. R., Rodger, C. J., & Clilverd, M. A. (2013). POES satellite observations of EMIC-wave driven relativistic electron precipitation during 1998–2010. Journal of Geophysical Research: Space Physics, 118(1), 232–243. https://doi.org/10.1029/2012ja017998
- Chen, Y., Reeves, G. D., & Friedel, R. H. (2007). The energization of relativistic electrons in the outer Van Allen radiation belt. *Nature Physics*, 3(9), 614–617. https://doi.org/10.1038/nphys655
- Codrescu, M. V., Fuller-Rowell, T. J., Roble, R. G., & Evans, D. S. (1997). Medium energy particle precipitation influences on the mesosphere and lower thermosphere. *Journal of Geophysical Research*, 102(A9), 19977–19987. https://doi.org/10.1029/97JA01728
- Crew, A. B., Spence, H. E., Blake, J. B., Klumpar, D. M., Larsen, B. A., O'Brien, T. P., et al. (2016). First multipoint in situ observations of electron microbursts: Initial results from the NSF FIREBIRD II mission. *Journal of Geophysical Research: Space Physics*, 121(6), 5272–5283. https://doi.org/10.1002/2016ia022485
- Dai, Y.-H. (2002). Convergence properties of the BFGS algorithm. SIAM Journal on Optimization, 13(3), 693-701. https://doi.org/10.1137/s1052623401383455
- Dwyer, J. R. (2004). Implications of x-ray emission from lightning. Geophysical Research Letters, 31(12), L12102. https://doi.org/10.1029/2004GL019795
- Engebretson, M., Lessard, M., Bortnik, J., Green, J., Horne, R. B., Detrick, D., et al. (2008). Pc1–Pc2 waves and energetic particle precipitation during and after magnetic storms: Superposed epoch analysis and case studies. *Journal of Geophysical Research*, 113(A1), A01211. https://doi.org/10.1029/2007ia012362
- Ersmark, T., Carlson, P., Daly, E., Fuglesang, C., Gudowska, I., Nieminen, P., et al. (2007). Geant4 Monte Carlo simulations of the galactic cosmic ray radiation environment on-board the international space station/Columbus. *IEEE Transactions on Nuclear Science*, 54(5), 1854–1862. https://doi.org/10.1109/tns.2007.906276
- Fang, X., Randall, C. E., Lummerzheim, D., Solomon, S. C., Mills, M. J., Marsh, D. R., et al. (2008). Electron impact ionization: A new parameterization for 100 eV to 1 MeV electrons. *Journal of Geophysical Research*, 113(A9), A09311. https://doi.org/10.1029/2008ja013384
- Fang, X., Randall, C. E., Lummerzheim, D., Wang, W., Lu, G., Solomon, S. C., & Frahm, R. A. (2010). Parameterization of monoenergetic electron impact ionization. *Geophysical Research Letters*, 37(22), L22106. https://doi.org/10.1029/2010g1045406
- Fox, N., & Burch, J. L. (2014). The Van Allen probes mission. Springer Science & Business Media.
- Frahm, R., Winningham, J., Sharber, J., Link, R., Crowley, G., Gaines, E., et al. (1997). The diffuse aurora: A significant source of ionization in the middle atmosphere. *Journal of Geophysical Research*, 102(D23), 28203–28214. https://doi.org/10.1029/97jd02430
- Frank, L., & Ackerson, K. (1971). Observations of charged particle precipitation into the auroral zone. *Journal of Geophysical Research*, 76(16), 3612–3643. https://doi.org/10.1029/ja076i016p03612
- Fraser-Smith, A. C. (1972). Spectrum of the geomagnetic activity index Ap. Journal of Geophysical Research, 77(22), 4209–4220. https://doi.org/10.1029/ja077i022p04209
- Funke, B., Ball, W., Bender, S., Gardini, A., Harvey, V. L., Lambert, A., et al. (2016). HEPPA-II model-measurement intercomparison project: EPP indirect effects during the dynamically perturbed NH winter 2008/2009. *Atmospheric Chemistry and Physics Discussions*.
- Glauert, S. A., Horne, R. B., & Meredith, N. P. (2014). Three-dimensional electron radiation belt simulations using the BAS radiation belt model with new diffusion models for chorus, plasmaspheric hiss, and lightning-generated whistlers. *Journal of Geophysical Research: Space Physics*, 119(1), 268–289. https://doi.org/10.1002/2013ja019281
- Horne, R. B., Glauert, S. A., & Thorne, R. M. (2003). Resonant diffusion of radiation belt electrons by whistler-mode chorus. *Geophysical Research Letters*, 30(9), 1493. https://doi.org/10.1029/2003g1016963
- Horne, R. B., & Thorne, R. M. (2003). Relativistic electron acceleration and precipitation during resonant interactions with whistler-mode chorus. Geophysical Research Letters, 30(10), 1527. https://doi.org/10.1029/2003gl016973
- Horne, R. B., Thorne, R. M., Shprits, Y. Y., Meredith, N. P., Glauert, S. A., Smith, A. J., et al. (2005). Wave acceleration of electrons in the Van Allen radiation belts. *Nature*, 437(7056), 227–230. https://doi.org/10.1038/nature03939
- Imhof, W., Kilner, J., & Reagan, J. (1985). Morphological study of energetic electron precipitation events using the satellite bremsstrahlung x ray technique. *Journal of Geophysical Research*, 90(A2), 1543–1552. https://doi.org/10.1029/ja090ia02p01543

BERLAND ET AL. 23 of 25

- Imhof, W., Nakano, G., Johnson, R., & Reagan, J. (1974). Satellite observations of bremsstrahlung from widespread energetic electron precipitation events. *Journal of Geophysical Research*, 79(4), 565–574. https://doi.org/10.1029/ja079i004p00565
- Inan, U., Shafer, D., Yip, W., & Orville, R. (1988). Subionospheric VLF signatures of nighttime D region perturbations in the vicinity of lightning discharges. *Journal of Geophysical Research*, 93(A10), 11455–11472. https://doi.org/10.1029/ja093ia10p11455
- Ivanchenko, V., Apostolakis, J., Bagulya, A. V., Abdelouahed, H. B., Black, R., Bogdanov, A., et al. (2011). Recent improvements in Geant4 electromagnetic physics models and interfaces. Progress in nuclear science and technology, 2(0), 898–903. https://doi.org/10.15669/pnst.2.898
- Ivanchenko, V., Incerti, S., Allison, J., Bagulya, A., Brown, J., Champion, C., et al. (2014). Geant4 electromagnetic physics: Improving simulation performance and accuracy. In SNA + MC 2013-Joint International Conference on Supercomputing in Nuclear Applications + Monte Carlo (p. 03101)
- Ivanchenko, V., Kadri, O., Maire, M., & Urban, L. (2010). Geant4 models for simulation of multiple scattering. *Journal of Physics: Conference Series*, 219(3), 032045. https://doi.org/10.1088/1742-6596/219/3/032045
- Johnson, A., Shumko, M., Griffith, B., Klumpar, D. M., Sample, J., Springer, L., et al. (2020). The FIREBIRD-II CubeSat mission: Focused investigations of relativistic electron burst intensity, range, and dynamics. Review of Scientific Instruments, 91(3), 034503. https://doi. org/10.1063/1.5137905
- Khazanov, G. V., & Chen, M. W. (2021). Why atmospheric backscatter is important in the formation of electron precipitation in the diffuse aurora. Journal of Geophysical Research: Space Physics, 126(5), e2021JA029211. https://doi.org/10.1029/2021JA029211
- Khazanov, G. V., Robinson, R., Zesta, E., Sibeck, D., Chu, M., & Grubbs, G. (2018). Impact of precipitating electrons and magnetosphere-ionosphere coupling processes on ionospheric conductance. Space Weather, 16(7), 829–837. https://doi.org/10.1029/2018sw001837
- Kim, Y.-K., Hwang, W., Weinberger, N., Ali, M., & Rudd, M. E. (1997). Electron-impact ionization cross sections of atmospheric molecules. The Journal of Chemical Physics, 106(3), 1026–1033. https://doi.org/10.1063/1.473186
- Koch, H., & Motz, J. (1959). Bremsstrahlung cross-section formulas and related data. Reviews of Modern Physics, 31(4), 920–955. https://doi.org/10.1103/revmodphys.31.920
- Köhn, C., & Ebert, U. (2014). Angular distribution of bremsstrahlung photons and of positrons for calculations of terrestrial gamma-ray flashes and positron beams. *Atmospheric Research*, 135, 432–465. https://doi.org/10.1016/j.atmosres.2013.03.012
- Krause, L. H. (1998). The interaction of relativistic electron beams with the near-Earth space environment. University of Michigan.
- LaBelle, J., & Treumann, R. (1988). Plasma waves at the dayside magnetopause. Space Science Reviews, 47(1-2), 175-202. https://doi.org/10.1007/bf00223240
- Lam, M. M., Horne, R. B., Meredith, N. P., Glauert, S. A., Moffat-Griffin, T., & Green, J. C. (2010). Origin of energetic electron precipitation> 30 KeV into the atmosphere. *Journal of Geophysical Research*, 115(A4), A00F08. https://doi.org/10.1029/2009ja014619
- Li, X., & Temerin, M. A. (2001). The electron radiation belt. Space Science Reviews, 95(1–2), 569–580. https://doi.org/10.1023/a:1005221108016
 Liu, H.-L., Bardeen, C. G., Foster, B. T., Lauritzen, P., Liu, J., Lu, G., et al. (2018). Development and validation of the whole atmosphere community climate model with thermosphere and ionosphere extension (WACCM-X 2.0). Journal of Advances in Modeling Earth Systems, 10(2), 381–402. https://doi.org/10.1002/2017ms001232
- Lorence, L., Jr., & Morel, J. (1992). CEPXS/ONELD: A one-dimensional coupled electron-photon discrete ordinates code package (Tech. Rep.).
 Lyons, L. R., Thorne, R. M., & Kennel, C. F. (1972). Pitch-angle diffusion of radiation belt electrons within the plasmasphere. *Journal of Geophysical Research*, 77(19), 3455–3474. https://doi.org/10.1029/ja077i019p03455
- Mark, T. (1982). Fundamental aspects of electron impact ionization. International Journal of Mass Spectrometry and Ion Physics, 45, 125–145. https://doi.org/10.1016/0020-7381(82)80103-4
- Marshall, R. A., & Bortnik, J. (2018). Pitch angle dependence of energetic electron precipitation: Energy deposition, backscatter, and the bounce loss cone. *Journal of Geophysical Research: Space Physics*, 123(3), 2412–2423. https://doi.org/10.1002/2017JA024873
- Marshall, R. A., & Cully, C. M. (2020). Atmospheric effects and signatures of high-energy electron precipitation. In *The dynamic loss of Earth's radiation belts* (pp. 199–255). Elsevier.
- Marshall, R. A., Xu, W., Woods, T., Cully, C., Jaynes, A., Randall, C., et al. (2020). The AEPEX mission: Imaging energetic particle precipitation in the atmosphere through its bremsstrahlung x-ray signatures. *Advances in Space Research*, 66(1), 66–82. https://doi.org/10.1016/j.asr.2020.03.003
- McPherron, R. L. (1979), Magnetospheric substorms. Reviews of Geophysics, 17(4), 657-681, https://doi.org/10.1029/rg017i004p00657
- Melnikov, Y. A. (1977). Some applications of the greens' function method in mechanics. *International Journal of Solids and Structures*, 13(11), 1045–1058. https://doi.org/10.1016/0020-7683(77)90075-0
- Millan, R., & Baker, D. (2012). Acceleration of particles to high energies in Earth's radiation belts. Space Science Reviews, 173(1-4), 103-131. https://doi.org/10.1007/s11214-012-9941-x
- Millan, R., McCarthy, M., Sample, J., Smith, D., Thompson, L., McGaw, D., et al. (2013). The balloon array for RBSP relativistic electron losses (BARREL). In *The Van Allen probes mission* (pp. 503–530). Springer.
- Mironova, I. A., Aplin, K. L., Arnold, F., Bazilevskaya, G. A., Harrison, R. G., Krivolutsky, A. A., et al. (2015). Energetic particle influence on the Earth's atmosphere. *Space Science Reviews*, 194(1–4), 1–96. https://doi.org/10.1007/s11214-015-0185-4
- Mori, K., Hailey, C., Bridges, G., Mandel, S., Garvin, A., Grefenstette, B., et al. (2022). Observation and origin of non-thermal hard x-rays from Jupiter. *Nature Astronomy*, 6(4), 442–448. https://doi.org/10.1038/s41550-021-01594-8
- Ni, B., Thorne, R. M., Zhang, X., Bortnik, J., Pu, Z., Xie, L., et al. (2016). Origins of the Earth's diffuse auroral precipitation. Space Science Reviews, 200, 205–259. https://doi.org/10.1007/s11214-016-0234-7
- Omura, Y., Miyashita, Y., Yoshikawa, M., Summers, D., Hikishima, M., Ebihara, Y., & Kubota, Y. (2015). Formation process of relativistic electron flux through interaction with chorus emissions in the Earth's inner magnetosphere. *Journal of Geophysical Research: Space Physics*, 120(11), 9545–9562. https://doi.org/10.1002/2015JA021563
- Patrick, M. R. (2022). Measuring energetic electron precipitation using high altitude balloons and x-ray spectroscopy (PhD Thesis). University of Calgary.
- Picone, J., Hedin, A., Drob, D. P., & Aikin, A. (2002). NRLMSISE-00 empirical model of the atmosphere: Statistical comparisons and scientific issues. *Journal of Geophysical Research*, 107(A12), SIA15-1–SIA15-16. https://doi.org/10.1029/2002ja009430
- Pytte, T., Trefall, H., Kremser, G., Jalonen, L., & Riedler, W. (1976). On the morphology of energetic (≥30kev) electron precipitation during the growth phase of magnetospheric substorms. *Journal of Atmospheric and Terrestrial Physics*, 38(7), 739–755. https://doi.org/10.1016/0021-9169(76)90112-4
- Ridley, A., Gombosi, T. I., & DeZeeuw, D. (2004). Ionospheric control of the magnetosphere: Conductance. In *Annales Geophysicae* (Vol. 22, pp. 567–584). https://doi.org/10.5194/angeo-22-567-2004
- Roble, R., & Ridley, E. (1987). An auroral model for the NCAR thermospheric general circulation model (TGCM). In Annales Geophysicae (Vol. 5, pp. 369–382).

BERLAND ET AL. 24 of 25

- Rodger, C. J., Clilverd, M. A., Thomson, N. R., Gamble, R. J., Seppälä, A., Turunen, E., et al. (2007). Radiation belt electron precipitation into the atmosphere: Recovery from a geomagnetic storm. *Journal of Geophysical Research*, 112(A11), A11307. https://doi.org/10.1029/2007ja012383
 Schwenn, R. (2006). Space weather: The solar perspective. *Living Reviews in Solar Physics*, 3(1), 1–72. https://doi.org/10.12942/lrsp-2006-2
- Selesnick, R. S., Looper, M. D., & Albert, J. M. (2004). Low-altitude distribution of radiation belt electrons. *Journal of Geophysical Research*, 109(A11), A11209. https://doi.org/10.1029/2004JA010611
- Seltzer, S. M., & Berger, M. J. (1986). Bremsstrahlung energy spectra from electrons with kinetic energy 1 KeV-10 GeV incident on screened nuclei and orbital electrons of neutral atoms with z= 1-100. *Atomic Data and Nuclear Data Tables*, 35(3), 345-418. https://doi.org/10.1016/0092-640x(86)90014-8
- Seppälä, A., Douma, E., Rodger, C., Verronen, P., Clilverd, M. A., & Bortnik, J. (2018). Relativistic electron microburst events: Modeling the atmospheric impact. *Geophysical Research Letters*, 45(2), 1141–1147. https://doi.org/10.1002/2017gl075949
- Seppälä, A., Verronen, P. T., Clilverd, M. A., Randall, C. E., Tamminen, J., Sofieva, V., et al. (2007). Arctic and Antarctic polar winter NOx and energetic particle precipitation in 2002–2006. Geophysical Research Letters, 34(12), L12810. https://doi.org/10.1029/2007gl029733
- Sergeev, V., Sazhina, E., Tsyganenko, N., Lundblad, J., & Søraas, F. (1983). Pitch-angle scattering of energetic protons in the magnetotail current sheet as the dominant source of their isotropic precipitation into the nightside ionosphere. *Planetary and Space Science*, 31(10), 1147–1155. https://doi.org/10.1016/0032-0633(83)90103-4
- Shprits, Y. Y., Subbotin, D. A., Meredith, N. P., & Elkington, S. R. (2008). Review of modeling of losses and sources of relativistic electrons in the outer radiation belt II: Local acceleration and loss. *Journal of Atmospheric and Solar-Terrestrial Physics*, 70(14), 1694–1713. https://doi. org/10.1016/j.jastp.2008.06.014
- Shumko, M., Sample, J., Johnson, A., Blake, B., Crew, A., Spence, H., et al. (2018). Microburst scale size derived from multiple bounces of a microburst simultaneously observed with the FIREBIRD-II CubeSats. *Geophysical Research Letters*, 45(17), 8811–8818. https://doi.org/10.1029/2018g1078925
- Sinnhuber, M., Nieder, H., & Wieters, N. (2012). Energetic particle precipitation and the chemistry of the mesosphere/lower thermosphere. Surveys in Geophysics, 33(6), 1281–1334. https://doi.org/10.1007/s10712-012-9201-3
- Solomon, S. C. (2001). Auroral particle transport using Monte Carlo and hybrid methods. *Journal of Geophysical Research*, 106(A1), 107–116. https://doi.org/10.1029/2000JA002011
- Stakgold, I., & Holst, M. J. (2011). Green's functions and boundary value problems. John Wiley & Sons.
- Summers, D., & Thorne, R. M. (2003). Relativistic electron pitch-angle scattering by electromagnetic ion cyclotron waves during geomagnetic storms. *Journal of Geophysical Research*, 108(A4), 1143. https://doi.org/10.1029/2002ja009489
- Tapping, K. (2013). The 10.7 cm solar radio flux (f10. 7). Space Weather, 11(7), 394-406. https://doi.org/10.1002/swe.20064
- Thorne, R. M. (1980). The importance of energetic particle precipitation on the chemical composition of the middle atmosphere. *Pure and Applied Geophysics*, 118(1), 128–151, https://doi.org/10.1007/bf01586448
- Tinslay, J., Faddegon, B., Perl, J., & Asai, M. (2007). SU-FF-T-447: Verification of bremsstrahlung splitting in Geant4 for radiotherapy quality beams. *Medical Physics*, 34(6Part14), 2504. https://doi.org/10.1118/1.2761172
- Tobiska, W. K., Bouwer, D., Smart, D., Shea, M., Bailey, J., Didkovsky, L., et al. (2016). Global real-time dose measurements using the automated radiation measurements for aerospace safety (ARMAS) system. Space Weather, 14(11), 1053–1080. https://doi.org/10.1002/2016sw001419
- Tobiska, W. K., Halford, A. J., & Morley, S. K. (2022). Increased radiation events discovered at commercial aviation altitudes. arXiv preprint arXiv:2209.05599
- Truscott, P., Lei, F., Dyer, C., Ferguson, C., Gurriaran, R., Nieminen, P., et al. (2000). Geant4-a new Monte Carlo toolkit for simulating space radiation shielding and effects. In 2000 IEEE radiation effects data workshop. Workshop record. Held in Conjunction with IEEE Nuclear and Space Radiation Effects Conference (cat. no. 00th8527) (pp. 147–152).
- Tsurutani, B. T., Lakhina, G. S., & Verkhoglyadova, O. P. (2013). Energetic electron (>10 KeV) microburst precipitation, ~5–15 s x-ray pulsations, chorus, and wave-particle interactions: A review. *Journal of Geophysical Research: Space Physics*, 118(5), 2296–2312. https://doi.org/10.1002/jgra.50264
- Urban, L. (2002). Multiple scattering model in Geant4. (Tech. Rep.).
- Whittaker, I. C., Gamble, R. J., Rodger, C. J., Clilverd, M. A., & Sauvaud, J.-A. (2013). Determining the spectra of radiation belt electron losses: Fitting demeter electron flux observations for typical and storm times. *Journal of Geophysical Research: Space Physics*, 118(12), 7611–7623. https://doi.org/10.1002/2013ja019228
- Xu, W., & Marshall, R. A. (2019). Characteristics of energetic electron precipitation estimated from simulated bremsstrahlung x-ray distributions. Journal of Geophysical Research: Space Physics, 124(4), 2831–2843. https://doi.org/10.1029/2018ja026273
- Xu, W., Marshall, R. A., Fang, X., Turunen, E., & Kero, A. (2018). On the effects of bremsstrahlung radiation during energetic electron precipitation. *Geophysical Research Letters*, 45(2), 1167–1176. https://doi.org/10.1002/2017g1076510
- Xu, W., Marshall, R. A., & Tobiska, W. K. (2021). A method for calculating atmospheric radiation produced by relativistic electron precipitation. Space Weather, 19(12), e2021SW002735, https://doi.org/10.1029/2021sw002735
- Xu, W., Marshall, R. A., Tyssøy, H. N., & Fang, X. (2020). A generalized method for calculating atmospheric ionization by energetic electron precipitation. *Journal of Geophysical Research: Space Physics*, 125(11), e2020JA028482. https://doi.org/10.1029/2020ja028482
- Zhang, X.-J., Angelopoulos, V., Mourenas, D., Artemyev, A., Tsai, E., & Wilkins, C. (2022). Characteristics of electron microburst precipitation based on high-resolution Elfin measurements. *Journal of Geophysical Research: Space Physics*, 127(5), e2022JA030509. https://doi.org/10.1029/2022ja030509

BERLAND ET AL. 25 of 25